UNIVERSITÀ DEGLI STUDI DI MESSINA

DIPARTIMENTO DI INGEGNERIA

CORSO DI DOTTORATO DI RICERCA IN INGEGNERIA E CHIMICA DEI MATERIALI E DELLE COSTRUZIONI
XXXVI CICLO
SSD: ING-IND/14 Progettazione Meccanica e Costruzione di Macchine

DIFFERENTIAL ENTROPY-BASED ANALYSIS OF POINT CLOUDS: NOVEL APPLICATIONS AND METHODS

Dottorando:
Emmanuele Barberi

Coordinatore:
Prof. Edoardo Proverbio

Tutor:
Prof. Eugenio Guglielmino (ING-IND/14)

Co-Tutor:
Prof. Filippo Cucinotta (ING-IND/15)

Anno Accademico
2022/2023

CONTENTS

LIST OF FIGURES

LIST OF TABLES

ABSTRACT

Point clouds are three-dimensional (3D) representations generated from data acquired through various technologies, including 3D scanners, advanced cameras, and depth sensors. These representations have brought about significant advancements in numerous sectors, such as autonomous driving, augmented reality, and Industry 4.0. In the modern industrial landscape, point clouds play an indispensable role. They are instrumental in real-time monitoring and optimization of production processes, enhancing the analysis of machine and robot performance. These 3D representations also facilitate the manipulation and training of industrial robots, enabling them to recognise objects and collaborate safely with humans. Additionally, point clouds are of paramount significance in industrial quality control, enabling the verification of product specifications against predefined criteria. The versatility of point clouds extends to representing systems of objects that can be simplified as points on a plane or in space. A wide array of analyses and applications can be conducted using point clouds. The focus of this study was on point cloud analysis based on differential entropy, a concept that quantifies the information contained in the data. Differential entropy of a point cloud provides insights into the spatial distribution of points. In this work, a thorough examination of this concept led to the development of three primary innovations: a novel formulation of differential entropy for point clouds, the creation of a new method called Differential Entropy for Deviation Analysis (*DEDA*), which is geared towards the analysis of geometric deviation for quality control in industrial production, and the introduction of the Differential Entropy-based Compactness Index (*DECI*), a compactness index designed specifically for analysing systems that can be schematised as point clouds, with a particular focus on the transportation

system, proposed as a risk index. The modification of the formulation of differential entropy for univariate and multivariate normal distributions has eliminated problems associated with the vanishing determinant of the covariance matrix, as present in the formula, and ensured that the entropic contribution of each point in the point cloud assumes a zero or positive value. This new formulation has paved the way for the development and demonstrated the effectiveness of the *DEDA* method and the *DECI* index. In the field of quality control, the *DEDA* method has proven to be reliable and robust. Geometric deviation analysis on samples produced through Additive Manufacturing (AM), conducted using both traditional methods based on Euclidean distance calculations between points in compared point clouds and the new *DEDA* method, have underscored the potential of the newly proposed method. The *DEDA* method, notably, provides a synthetic quality index that determines the product's quality level, as opposed to traditional methods that rely on the interpretation of mean and standard deviation, which can often lead to challenging or incorrect quality level assessments. Furthermore, the robustness assessment of the *DEDA* method has demonstrated its ability to overcome several limitations inherent in classical methods, including the presence of holes, background noise, density variations between compared point clouds, and the non-commutativity of Euclidean distance. The *DEDA* method also lays the foundation for the development of a new point clouds registration method. The latest innovation, the *DECI* index, allows for the derivation of a descriptive index of the compactness of a point cloud. While this index is suitable for various applications, it has been applied to monitor maritime traffic, serving as a quantifiable measure of risk in a specific sea area. Leveraging information on maritime traffic, *DECI* values were evaluated on an hourly, monthly, and annual basis. This enabled a comprehensive examination of maritime traffic, shedding light on the most and least congested time periods. *DECI*-based analysis could be instrumental in implementing measures to

alleviate congestion in the busiest sea areas and facilitating qualitative comparisons.

Keywords: Point Clouds, Entropy, Differential Entropy, Registration, ICP, 3D Scans, Reverse Engineering, Quality Control, Deviation Analysis, Computer Vision, Compactness Index, 3D Printing.

Highlights:

- New formulation of differential entropy specifically tailored for point clouds.
- Quality control method based on differential entropy, designed to overcome limitations found in existing approaches.
- Compactness index for analysing systems that can be represented as point clouds.
- Case studies to showcase the potential of the introduced novelties.

1 INTRODUCTION

1.1 Overview of Point Clouds

In the landscape of advanced technologies, point clouds constitute one of the most invaluable assets for comprehending, analysing, and engaging with the physical world in an increasingly sophisticated manner. These intricate three-dimensional (3D) representations, crafted from sets of data points, have evolved into a fundamental cornerstone of state-of-the-art digital applications, significantly reshaping our perception of our interaction with the physical world. Point clouds essentially serve as highly detailed 3D mappings of actual objects, environments, and landscapes. They are generated using a diverse array of technologies, including 3D scanners, advanced cameras, and depth sensors. Each data point within a point cloud corresponds to a precise location within 3D space, meticulously capturing coordinates (x, y, z) and often encompassing supplementary attributes such as colour and intensity. This dataset enables the faithful digital recreation of the real world in a profoundly detailed format.

The widespread proliferation of this technology has paved the way for a wide spectrum of applications across various industries. One of the most conspicuous domains is autonomous driving, where point clouds are pivotal in enabling vehicles to meticulously perceive their surroundings and make real-time decisions. Nevertheless, their sphere of influence extends far beyond mobility, permeating fields such as augmented reality, where point clouds facilitate the superimposition of virtual objects onto the tangible world with unparalleled precision.

As a component of Industry 4.0, a paradigm embracing the digitalization and advanced automation of industrial processes, point clouds assume a pivotal role. These 3D representations are leveraged to monitor and optimise production processes in real-time, facilitating the analysis of machinery and robot performance. Point clouds processing enhances the manipulation and training of industrial robots, empowering them to recognise objects, precisely compute trajectories, and securely collaborate with humans in the factories of the future. Moreover, point clouds feature prominently in quality control within industrial manufacturing, enabling the verification of product specifications against predefined criteria. Anchored in detailed point cloud data, this quality control process guarantees alignment with the requisite quality standards. Point clouds, besides furnishing a detailed representation of the physical realm, present a unique opportunity for innovative data analysis and interpretation. Advanced point cloud processing can unveil hitherto concealed information, discern intricate patterns, and facilitate advanced decision-making.

1.2 Objective of the thesis

During this thesis, an in-depth study was conducted on differential entropy and on the analyses carried out using this measure on point clouds, with the aim of extracting information about the geometry they represent. This research resulted in the development of a new method for analysing geometric deviation in quality control and the establishment of a compactness index with multiple potential applications. Therefore, the objective of this thesis is to present the modifications made to the formulation of differential entropy and, specifically, to demonstrate the innovative methods derived from these modifications, validating them through case studies.

1.3 Outline

In the introductory chapter, an overview of what point clouds entail, their characteristics, and the various sectors in which they find application is provided. The second section, titled "State of the Art," presents all the fundamental concepts essential for a thorough understanding of the innovations introduced. This section covers key aspects such as the primary acquisition methods, the data capture process, the analyses conducted through differential entropy, and the assessment of geometric deviation. The third section, "Materials and Methods," introduces the innovations presented in this work initially and then delves into them in detail, aided by practical applications and case studies. Conclusions will follow, summarizing the work and the results obtained.

1.4 Introduction to Point Clouds

1.4.1 Definition

Point clouds are a form of digital representation that provide a detailed portrait of real-world objects and environments within 3D space. In the context of engineering and computer science, they are often thought of as a collection of data points distributed in the 3D Euclidean space, where each point serves as an anchor point, indicating an exact location in the physical world. The minimum attributes of a point within a point cloud are typically its spatial coordinates (x, y, z), which capture its precise position relative to a chosen coordinate system. The versatility of point clouds extends beyond their spatial coordinates. These data points can carry a number of additional attributes, enriching the information they convey. One of the most common additional attributes is colour, which improves the visual quality and realism of point clouds. Colour information is typically represented using the Red-Green-Blue (RGB) model, where each channel (R, G, and B) defines the intensity of a particular colour component. With values ranging from 0 to 255 for each channel, this model allows for the generation of a wide range of colours. Incorporating colour information into point clouds is invaluable in applications such as digital 3D modelling, where realistic rendering of objects and scenes is of paramount importance.

Another noteworthy attribute associated with point clouds is intensity. Intensity values, typically between 0 and 1, convey information about the reflectance or brightness of a point. This attribute is particularly useful in laser-based scanning techniques, such as LiDAR (Light Detection and Ranging), in which sensors measure the intensity of the returned laser signal. By analysing intensity data, it becomes possible to differentiate various materials, surfaces, or objects based on their reflection properties. This capability has far-reaching implications, including applications in environmental monitoring, forestry, and autonomous navigation. Furthermore, each point within a point cloud can have normal vectors (i, j, k) as attributes. These normal vectors provide information about the orientation of surfaces at each point, aiding in tasks such as surface reconstruction, shading, and curvature analysis. The inclusion of normal vectors is crucial in applications such as 3D graphics and computer-aided design, where understanding surface characteristics and interactions is essential for realistic simulations and modelling. **Figure 1** shows a generic point cloud in the 3D space and its main attributes.

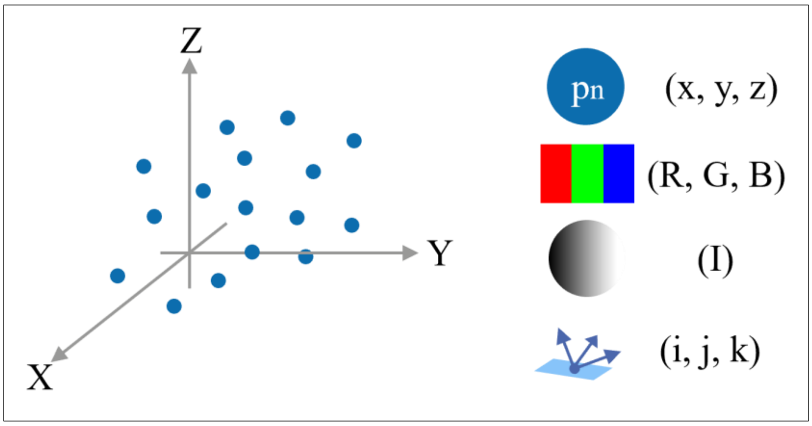

Figure 1. Example of a point cloud and its main attributes.

Thus, point clouds serve as intricate digital snapshots of the physical world, capturing not only spatial coordinates but also additional attributes such as colour, intensity, and normal vectors. These attributes, whether applied for visual fidelity or greater analytical depth, enhance the ability of point clouds to capture the complexity and richness of real-world scenes. Point clouds are a foundational technology with applications spanning fields such as geospatial analytics, robotics, computer vision, and more. Their ability to capture, store, and represent detailed 3D data ensures they remain indispensable in our increasingly digital and interconnected world.

1.4.2 Fields of application

Point clouds, with their capacity to capture detailed 3D data, find extensive utility in various fields. Their versatility and precision render them invaluable resources for multiple applications, significantly contributing to enhanced comprehension and innovation across diverse industries.

Product design

Point clouds are utilised in the creation of digital models representing real objects or environments. These models are acquired through various acquisition techniques that capture a substantial volume of data in the form of points. Subsequently, this data can be processed and applied, for instance, both to generate Computer Aided Design (CAD) models, through a specific process, that replicate the geometry of the original objects and to analyse their shape. The resulting CAD models hold significant value across numerous contexts, including the manufacturing industry, where they can be employed to redesign or enhance existing components without the need to start from scratch. This process is referred to as *geometric reverse engineering*. Point clouds also play a crucial role in quality control. Following the production of a component, it undergoes scanning, and the acquired point clouds are compared to the reference model in a process known as *deviation analysis*. This comparison enables the evaluation of any deviations or production defects in the component's shape, size, or position relative to the required specifications. In this manner, point cloud-based quality control ensures that products meet stringent quality and precision standards. Moreover, the triangulation process, by the means, for instance, of Delaunay method, allows to obtain the surface of the scanned object. This surface can be used to obtain a mesh useful for Computed Aided Engineering (CAE) analysis such as Finite Elements Methods (FEM) and Computational Fluid-Dynamics (CFD).

Mixed Reality

Point clouds are an invaluable resource for creating immersive virtual worlds and experiencing Augmented Reality (AR) [1], Virtual Reality (VR) [2], and Augmented Virtuality (AV) [3]. Their ability to capture 3D details with extreme precision provides a solid foundation for constructing lifelike virtual environments and engaging interactive applications. In this context, point clouds allow users to explore and interact with the physical world enriched with virtual elements. This creates engaging and interactive educational experiences making AR particularly effective in sectors such as education and professional training. Simultaneously, in Virtual Reality (VR) and Augmented Virtuality (AV), for example, in the context of corporate training, an acquired point cloud can serve as the foundation for creating realistic training scenarios [4,5]. Companies can utilise these instruments to train employees on complex machinery or industrial processes, enabling them to interact with realistic virtual models. Users can be immersed in virtual environments that precisely replicate the physical characteristics of the real world, allowing them to practice in realistic and safe conditions. Consider, for example, planning a maintenance intervention in areas of a factory where environmental conditions are adverse (due to noise or temperatures), to test the intervention in a secure environment to enhance efficiency and reduce the time spent at the site of the operation.

Autonomous driving

Point clouds are assuming an increasingly significant role in the field of autonomous driving [6], which currently relies primarily on artificial vision via cameras [7,8]. This revolutionises how autonomous vehicles perceive and understand their surrounding environment, enabling them to 'see' the world with a higher level of detail and precision. This advancement paves the way for enhanced road safety and more efficient driving. Point clouds acquired through these sensors empower autonomous vehicles to create a detailed map of their surroundings, including vehicles, pedestrians, obstacles, and more [9]. Point cloud analysis is crucial for real-time interpretation of the road environment. Autonomous vehicles employ advanced algorithms for object recognition, trajectory tracking, and decision-making based on this data [10]. This process, known as “Simultaneous Localization and Mapping” (SLAM) [11], enables autonomous vehicles to accurately determine their position on the road and adapt to environmental changes in real time. The integration of point clouds in autonomous driving is redefining the future of mobility, and with ongoing advancements and refinements in sensors and algorithms, they will remain central to the evolution of autonomous driving and future mobility.

Medicine

The utilisation of point clouds in the medical field is revolutionising the visualisation and planning of surgical procedures, offering fresh perspectives for precise diagnosis and effective treatment. Point clouds have displayed substantial potential in the 3D reconstruction of anatomical objects from DICOM (Digital Imaging and Communications in Medicine) medical images. This process enables medical practitioners to obtain a 3D representation of patients' internal organs and tissues. Such representation provides a clear view of anomalies or lesions, empowering medical professionals to make more accurate diagnoses. A significant application of this technology is the 3D printing of customised anatomical models [12,13]. By employing point clouds extracted from DICOM images [14], physical models of patient-specific organs can be manufactured. These models enable doctors to explore the internal structure of organs in a tactile manner, simulating intricate surgical procedures and meticulously planning interventions. A surgeon can employ a 3D model of an organ to strategize the operation through in vitro testing [15,16]. This approach allows for risk minimisation and optimisation of the intervention's outcome. Moreover, 3D models can serve educational purposes, offering medical students and young surgeons opportunities to acquire practical skills in a virtual environment before confronting real clinical scenarios. Numerous studies underscore how the combined usage of point clouds and Machine Learning (ML) techniques, particularly Deep Learning (DL), can contribute to the diagnosis and prognostication of post-operative outcomes and complications, as seen e.g., in the treatment of Abdominal Aortic Aneurysm through EndoVAscular Repair (EVAR) surgery [17]. The application of point clouds in diagnostic imaging and medicine is thus creating fresh avenues for enhanced patient care and a deeper comprehension of the anatomical and pathological facets of the human body.

Forensics

Point clouds are assuming an increasingly significant role in crime scene reconstruction and forensic investigations. Several studies show the use of 3D scans to document and analyse evidence collected at crime scenes, providing essential support for judicial investigations and case resolution. Another example of the application of point clouds in this context is comparative ballistics. This technique involves obtaining detailed 3D scans of shell casings recovered from crime scenes or shooting locations [18–22]. Advanced technologies, such as confocal microscopy, enable the capture of extremely high-resolution images of bullet casings, meticulously capturing microscopic details. The use of point clouds in ballistic analysis opens up new perspectives for forensic experts [23,24]. The precision and objectivity of the 3D data enable a more accurate comparison between cartridge cases and specific firearms [25]. This approach can be critical in establishing crucial connections in crime cases, assisting law enforcement in identifying the weapons involved in shootings or linking bullets to specific firearms. Point clouds are also proving to be particularly useful in autopsies and post-mortem investigations, where point clouds of organs and tissues can be acquired [26]. This data can be used to gain a better understanding of accident dynamics or the causes of a person's death. With the constant advancement of point cloud acquisition and analysis technologies, it is reasonable to hypothesise that their role in investigations will continue to expand, further enhancing the ability to shed light on crimes and incidents.

Cultural heritage

In the field of cultural heritage documentation, point clouds represent a valuable tool for the long-term preservation of archaeological findings, historic sites, and artworks. 3D scans enable the recording of every detail of structures and artworks, providing a robust foundation for future studies and research [27]. This digital data can be archived and shared with the scientific community and the public, contributing to the conservation of historical and cultural memory [28]. Moreover, point clouds are indispensable instruments for preventive conservation. They enable restorers to monitor the state of preservation of artworks over time, detecting any changes or damage. This ongoing monitoring allows for timely corrective or maintenance measures to be implemented for optimal preservation. Additionally, the combined use with AV, through the utilization of haptic feedback technology, currently under investigation, would make it possible to physically touch sculptures and other historical artefacts, an experience which is generally not feasible at present due to the potential for damage to the objects [29]. These innovative approaches to the documentation and preservation of cultural heritage significantly contribute to the comprehension and safeguarding of human history and art.

Topography

The extensive use of sensors for acquiring point clouds mounted on vehicles, drones, and fixed or mobile platforms, in conjunction with photogrammetric techniques, is employed to obtain topographical data of unparalleled precision and detail [30]. These detection systems generate exceptionally information-rich point clouds, precisely revealing the morphology of the terrain, buildings, vegetation, and other characteristics of the acquired environment. These point clouds offer intriguing opportunities for a wide range of applications. For instance, they make a substantial contribution to the creation of highly detailed maps, ushering in a new level of precision in territory representation [31]. These maps are indispensable for advanced navigation, natural resource management, infrastructure design, urban and land use planning, as they provide a comprehensive and accurate view of the environment under consideration.

Geology

3D scanning of geological formations, such as mountains, canyons, or caves, provides geologists with valuable information about the structure and evolution of the terrain [32]. This data is essential for planning engineering projects, such as the construction of dams, bridges, or tunnels, as it allows for a better understanding of the land's morphology and the evaluation of potential geological risks. Furthermore, point clouds are fundamental tools for managing natural risks, such as landslides, earthquakes, and floods. Detailed terrain mapping with point clouds enables the identification of risk areas and the implementation of preventive measures for public safety. In the context of scientific geological research, point clouds are used to study the evolution of natural phenomena over time. For example, it is possible to monitor changes in the morphology of a mountain or the deformation of a geological fault through periodic scans with point clouds [33]. These data contribute to the understanding of geological dynamics and the advancement of scientific knowledge in this field.

Precision agriculture

The 3D scanning of agricultural fields opens the door to a wide range of opportunities and benefits that help crop cultivation and management. The representation through point clouds, in fact, allows for an accurate evaluation of the vegetation [34]. Laser sensors can detect plant density and height very precisely. This data is essential for monitoring crop health, identifying early signs of plant stress or disease, and intervening promptly [35,36]. Farmers can also use this information to optimise the application of fertilisers, pesticides, and irrigation, minimising waste and maximising crop yields. A concrete example of how point clouds are transforming precision agriculture is the use of drones equipped with laser scanning systems [37]. These drones fly over agricultural fields and collect detailed 3D data, which is then analysed. Farmers can then make data-driven decisions and significantly improve the efficiency of their operations.

2 STATE OF THE ART

2.1 Point Clouds acquisition technologies

2.1.1 Light Detection And Ranging (LiDAR)

LiDAR is a remote sensing technology that has revolutionised the ability to measure and map environments. This technology is based on the use of laser to measure the distance between a LiDAR sensor and a certain object [38]. This fundamental principle enables high-precision 3D data collection, paving the way for a wide range of applications in various industries. The first studies on the development of this technology can be found in the early 20th century, but the first practical implementations emerged in the 1960s [39]. Since then, this technology has undergone advancements, with significant improvements in optical components and sensors. These advances have made LiDAR more accessible and versatile for a wide range of applications. Today, LiDAR is a key technology in many industries and is continuing to evolve with new innovations, such as more compact and lightweight sensors, as well as greater efficiency in data acquisition and processing [40]. Its growing importance is evident in the field of vehicle automation, where LiDAR plays a crucial role in environmental perception for autonomous vehicles [41]. What makes LiDAR so powerful is its ability to perform these measurements quickly and continuously, thus creating a real-time data stream or detailed 3D representation of the environment. Data acquisition can be based on two different operating principles: phase-shift and time-of-flight (TOF) [42].

In a LiDAR system employing TOF, a pulse of light is typically emitted from a pulsed laser diode, initiating an internal clock. This light pulse swiftly traverses the distance towards an object at nearly the speed of light until it makes contact with the object. A portion of the light then rebounds off the object, retracing its path back towards the LIDAR system at almost the speed of light, ultimately striking a photodetector. Upon reaching the photodetector, the light signals the clock, which had commenced when the initial pulse was emitted, to cease. By knowing the velocity of light and the time taken for the light to travel the round trip between the LIDAR system and the object, it is possible to precisely determine the distance to the object. On the other hand, time-of-flight LiDAR measures distance by calculating the time it takes for a laser pulse to go to the object of interest and return back to the sensor. This approach is known for its ability to acquire data at high speeds, making it ideal for real-time applications such as autonomous vehicles, drones, and other situations where responsiveness is critical. The distance d of the object is given by the formula [42]:

$$d = \frac{c \cdot t}{2} \tag{1}$$

Where:

- $c =$ speed of light
- $t =$ time it takes for the light to travel to the target and back.

In the phase-shift LiDAR a continuous source is utilised, with its power modulated at a consistent frequency. Photodetectors, in this context, serve a dual purpose. They not only ascertain the presence of light but also quantify its power. Consequently, a sine curve can be generated to represent the return signal. By analysing the phase difference, which signifies the variance in radians between the peaks of these waveforms, it is possible to determine the distance to the object. This phase change is caused by the change in wavelength of light as it travels through the air and hits the object. The distance d of the object is given by the formula [42]:

$$d = \frac{c \cdot \Delta\phi}{2\pi \cdot f} \tag{2}$$

Where:

- c is the speed of light
- $\Delta\phi$ is phase shift
- f is the frequency at which the power is modulated.

2.1.2 3D Structured-light Scanner

The structured light 3D scanner utilises structured light to initially capture a series of 3D points from an object. The underlying principle of this technology involves projecting structured light [43] patterns (typically bands or lines) onto the object to be scanned using a projector. These projected light patterns onto an object tend to deform based on the object's shape. The scanner is also equipped with a detection system, typically comprising one or two cameras, which capture the reflected light [44]. Subsequently, specialised algorithms, often based on triangulation, enable the software to reconstruct the object's geometry in the form of a point cloud. It is noteworthy that the point cloud is acquired only for the portion of the object exposed to the structured light. Consequently, considering the object's geometry, multiple acquisitions with relative rotations between the scanner and the object may be necessary. This can be accomplished by employing a turntable on which the object to be scanned is positioned, while the scanner remains stationary (e.g., for small and easily manipulable objects) or by keeping the object stationary and moving the scanner between scans (e.g., for larger objects). To accurately combine all partial point clouds obtained from each scan and derive a comprehensive point cloud representing the entire geometry of the scanned object, the scanner software employs registration (see chapter 2.2.3) techniques. In certain instances, markers, small stickers placed around or on the object, may be required for recognition by the acquisition system and to facilitate the spatial registration of the scans.

2.1.3 Microscopy

Microscopy is one of the techniques also used to obtain point clouds, with particular reference to its applications in the field of biology [45] and in the evaluation of the surface characteristics of materials [46]. The primary microscopy techniques employed to generate point clouds include confocal microscopy, focus variation microscopy, and interferometric microscopy.

Confocal microscopy is a technique enabling the acquisition of high-resolution 3D representation of material surfaces [47]. The procedure commences with the illumination of the sample via a laser beam meticulously focused on a specific region. An objective lens is employed to precisely direct the laser beam onto the material's surface and to gather the light reflected by the sample. An essential component of this system is the pinhole, positioned between the lens and the detector, which serves to exclude light originating from areas out of the focal plane, thus concentrating solely on the light emanating from the precise focal plane of the material. To generate a 3D representation of the material, the confocal microscope conducts a sequential scan along the x, y, and z axes. The laser beam horizontally traverses diverse positions on the material's surface and incrementally ascends vertically to capture data from varying depths. Throughout this scanning process, the microscope records the intensity of light reflected or emitted exclusively from the x-y grid points that are focused on the material's surface for each focal plane along the z-axis. The x-y coordinates of these focused points, coupled with the z coordinate of the focal plane, are then utilised to derive the 3D spatial coordinates of the points constituting the point cloud. This methodology enables the examination of morphological details, surface roughness, and other topographic characteristics of the material [48]. It is also used in biology field [49].

Focus variation microscopy exploits on the variation of the focus plane's position to gather information about the 3Dshape of a sample. The focus is adjusted, and the sample surface is examined at various focus positions. The resulting image enables the reconstruction of the sample's topography.

Confocal microscopy and focus variation both exhibit the optical sectioning property, showcasing similar depth focusing characteristics. The primary distinction lies in their proficiency: confocal microscopy is more adept at handling smooth surfaces, while focus variation microscopy excels in imaging very rough surfaces [50].

Interferometric microscopy leverages the principle of light interference to acquire detailed information about the structure and morphology of a sample. There are various variations of interferometric microscopy, with one of the most common being White Light Interferometry (WLI) microscopy or Low-Coherence Interferometry (LCI) microscopy. In this technique, broadband light (white light) or low-coherence light passes through or reflects off the sample. The light is split into two arms: one passing through the sample and the other serving as a reference. Subsequently, the light reflected or transmitted by the two arms is recombined, and the phase difference between the two light waves interferes, generating an interference pattern [51].

2.1.4 Photogrammetry

Photogrammetry is a technique that enables the generation of 3D representations of objects or environments by utilizing a series of photographs taken with a camera featuring a fixed lens. This methodology is founded on the principle of triangulation, which leverages variations in position and angles across photographs to compute the 3D coordinates of the points within the depicted object [52]. To obtain a 3D representation from two-dimensional (2D) photographs, it is imperative to capture a sequence of images of the object of interest from various angles (to ensure comprehensive coverage of the object, photographs should be taken in a 360-degree manner around the object). Specialised photogrammetry software, such as 3DF Zephyr (by 3DFLOW), employs algorithms designed to identify shared control points across different photographs and utilises triangulation algorithms. This software is capable of producing a 3D point cloud that accurately represents the photographed object or environment.

2.1.5 3D CAD Models

From the CAD models, it is possible to generate a point cloud that accurately represents the virtual object's geometry. Various software tools can be employed to extract points on the surface of these objects, which can then be exported in the form of a point cloud. The selection of points on the surface can follow a regular, random, or adaptive pattern. Adaptive sampling entails increasing the point cloud density in areas with complex geometry and decreasing it in areas with simpler geometry. When working with CAD models, extracting point clouds in this manner is often the initial step in obtaining meshes or surfaces, through a triangulation process.

2.1.6 Computed Tomography (CT)

Computed tomography (CT) is a sophisticated imaging modality employed in both medical and industrial domains to acquire 3D representations of internal objects or structures. CT relies on a series of X-rays or alternative radiation sources to capture a sequence of two-dimensional images or cross-sectional slices of an object. These images can subsequently undergo processing to generate a 3D portrayal of the object or the area of interest [53].

Within the realm of medicine, CT finds extensive utility in diagnosing and assessing a wide spectrum of medical conditions. For instance, it can yield intricate images of the brain, chest, abdomen, and various other anatomical regions. These 3D images facilitate the identification of lesions, tumours, bone fractures, anomalies, and other irregularities by medical practitioners [54]. In the industrial sector, CT predominantly serves the purpose of quality control and non-destructive inspection of materials [55]. This technique can unveil internal imperfections like air pockets, metallic inclusions, or fractures within materials. Commencing with 3D images, represented as voxels (volumetric pixels), the 3D analogue of pixels, it becomes feasible to derive the geometry of the object or the particular area of interest in the form of a point cloud. To accomplish this, specialised segmentation and reconstruction software designed for CT images must be employed. The resultant point cloud can then be employed for purposes such as measurements, analyses, simulations, and more, within both medical and industrial domains.

2.2 Point Clouds registration

2.2.1 Overview

In the context of point cloud registration, as previously said in chapter 2.1, pertaining to methodologies for acquiring point clouds, it is imperative to comprehend that the registration process assumes a pivotal role in the acquisition of point clouds that faithfully portray scans of objects or 3D environments. Throughout the acquisition process, data acquired through changes in angle measurement typically exhibits partial overlap and may manifest issues pertaining to rotational and translational misalignment. To construct a comprehensive 3D model, it becomes necessary to integrate and align this point cloud data. For instance, it is possible to undertake operations involving rotation and translation upon one set of point cloud data in order to conform it to the corresponding segment of another set of point cloud data.

The objective of the registration process, therefore, is to estimate the position and orientation of the distinct acquisitions, to insert them within a global coordinate system, and to merge the information such that regions of overlap integrate within a singular resultant point cloud. Through this method, therefore, a comprehensive 3D model of the target can be obtained. This point cloud registration process is indispensable across a spectrum of domains, with particular significance within the realms of reverse engineering and computer vision. Its significance arises from the imperative need to procure precise and uniform representations of the physical world in digital format [56].

In the context of its application, the registration of point clouds holds significant relevance across various domains, including robotics and computer vision. In recent times, owing to advancements in high-precision and automated 3D scanning technology, registration algorithms have gained paramount importance within the manufacturing sector. They are instrumental for tasks such as tolerance analysis, quality control, and reverse engineering [57].

2.2.2 Mathematical foundations

From a mathematical perspective, the registration of two point clouds (P and P'), considering a rigid transformation, with 6 Degrees of Freedom (DoF), entails obtaining a *transformation matrix* $\boldsymbol{T}$ that represents a roto-translation:

$$\boldsymbol{T} = \begin{bmatrix} r_{1,1} & r_{1,2} & r_{1,3} & t_1 \\ r_{2,1} & r_{2,2} & r_{2,3} & t_2 \\ r_{3,1} & r_{3,2} & r_{3,3} & t_3 \\ 0 & 0 & 0 & 1 \end{bmatrix} \tag{3}$$

Where:

- $r_{i,j}$ are the elements of the *rotation matrix* $\boldsymbol{R}$
- t_i are the elements of the *translation vector* $\boldsymbol{t}$.

Therefore, through a roto-translation, a generic point in space $p(x, y, z) \in P$, defined by its own coordinates, will be mapped to the point $p'(x', y', z') \in P'$ defined by another set of coordinates. Mathematically, it can be written:

$$\begin{bmatrix} x' \\ y' \\ z' \\ 1 \end{bmatrix} = \begin{bmatrix} r_{1,1} & r_{1,2} & r_{1,3} & t_1 \\ r_{2,1} & r_{2,2} & r_{2,3} & t_2 \\ r_{3,1} & r_{3,2} & r_{3,3} & t_3 \\ 0 & 0 & 0 & 1 \end{bmatrix} \begin{bmatrix} x \\ y \\ z \\ 1 \end{bmatrix} \tag{4}$$

And in its concise form:

$$\boldsymbol{p}' = \boldsymbol{T}\,\boldsymbol{p} \tag{5}$$

By separating the transformations into rotation and translation:

$$\begin{bmatrix} x' \\ y' \\ z' \end{bmatrix} = \begin{bmatrix} r_{1,1} & r_{1,2} & r_{1,3} \\ r_{2,1} & r_{2,2} & r_{2,3} \\ r_{3,1} & r_{3,2} & r_{3,3} \end{bmatrix} \begin{bmatrix} x \\ y \\ z \end{bmatrix} + \begin{bmatrix} t_1 \\ t_2 \\ t_3 \end{bmatrix} \tag{6}$$

$$\boldsymbol{p}' = \boldsymbol{R}\,\boldsymbol{p} + \boldsymbol{t} \tag{7}$$

2.2.3 Registration methods

In scientific literature it is possible to see that most of the existing registration methods are designed to minimise geometric projection errors through two distinct processes: correspondence searching and transformation estimation [58]. These two processes are carried out alternately until the geometric projection error reaches its minimum value. Once accurate correspondences are established, the transformation estimation can be obtained. In recent years, significant advancements have been made in 3D DL techniques [59–62]. These techniques are focused on extracting distinctive features from point clouds and identifying precise correspondences. Subsequently, these correspondences are utilised to estimate a transformation through a dedicated transformation estimation stage. Among all the point clouds registration methods, the Iterative Closest Point (ICP) algorithm remains the most commonly studied and used [63–68].

2.2.4 Iterative Closest Point (ICP) algorithms

ICP is an algorithm, developed by Besl and McKey [69] and by Chen and Medioni [70] in 1992, as a method for aligning, or register, a broad spectrum of objects, encompassing point clouds, polylines, faceted and curved surfaces, as well as implicit and parametric surfaces. There are two main methods to implement ICP: point-to-point [69] and point-to-plane [70].

The point-to-point ICP variant is employed when the direct alignment of point clouds is required, while the point-to-plane ICP variant is considered suitable in cases where a mixed representation involving points and surfaces or meshes exists. The selection between these two variants is contingent upon the nature of the data and the specific objectives of 3D alignment. In this thesis, emphasis will be placed on the point-to-point method due to its relevance to the novelties introduced.

The primary objective of the ICP algorithm lies in identifying a transformation matrix ($\boldsymbol{T}$), which achieves the optimal alignment between the *target* point cloud, to which the transformation will be applied, and the reference point cloud, often referred to as the *model*. This alignment process is based on minimizing a specific distance metric, typically the root mean square distance between points in the target point cloud and their corresponding points in the nearest model point cloud. ICP addresses the correspondence problem by working on the assumption that the scene is roughly aligned with the model, implying that each point in the scene corresponds to the closest point in the model. Given that ICP is an iterative descent algorithm, it necessitates a precise initial estimate to ensure convergence towards the global minimum. In cases where the two point clouds (target and model) are severely misaligned, there exists a possibility that the ICP algorithm will converge towards a local minimum, rather than the desired global minimum. This could result in unfavourable registration outcomes, as ICP may yield a suboptimal solution. For these reasons, in order to effectively tackle the registration problem with ICP when the point clouds are misaligned, it is crucial to initialise the iterative process with an initial transformation applied to the target point cloud. This initial transformation should position the target point cloud as closely as possible to the reference model.

Regarding the fundamental principle of the ICP algorithm, it encompasses the following process [71]:

1. Given two point clouds, model (A) and target (B) respectively, along with an initial transformation $\boldsymbol{T_I}$[1], the algorithm aims to identify the nearest corresponding reference point in A for each point in B, thus establishing pairs of corresponding points.
2. Subsequently, it computes the Euclidean distances between all pairs of corresponding points, utilizing a suitable measure of the error in the objective function.
3. To minimise this error, the algorithm employs Singular Value Decomposition (SVD) [72] to calculate the transformation $\boldsymbol{T_1}(\boldsymbol{R_1}, \boldsymbol{t_1})$[2] that minimise the error.
4. Upon obtaining the $\boldsymbol{R}$ and $\boldsymbol{t}$ transformations, the subsequent step involves transforming B based on these transformations and re-establishing the corresponding point pairs.
5. This process is iterated until satisfactory convergence is achieved[3], thereby obtaining the transformation $\boldsymbol{T}(\boldsymbol{R}, \boldsymbol{t})$ which, when applied to the point cloud B, ensures its best alignment with point cloud A.

This principle serves as the core of the ICP algorithm and its variants, enabling the accurate registration of 3D shapes. It is noteworthy that since the inception of ICP, numerous variations of the algorithm have been proposed. These variants aim to enhance various aspects, including execution speed and convergence quality when compared to the original algorithm. For instance,

---

[1] The software that implements the ICP algorithm essentially calculates the centroids of the point clouds and applies a transformation to align them if an initial transformation is not provided.

[2] The subscript refers to the first iteration.

[3] It is possible to set a minimum error value or a maximum number of iterations.

some variants combine multiple distance measures with local descriptors [73]. Nevertheless, both the ICP algorithm and its variants continue to yield robust results when the positions of the shapes to be aligned are in close proximity to each other [74]. In the context of ICP variants, one of the intriguing approaches is feature-based matching. This method entails transforming the original point clouds into a simplified representation, wherein high-level features (planes [75], line segments [76] and corners [77]) are found. This approach facilitates the identification of salient features within 3D data, thereby enhancing the reliability of position change estimation between two point clouds [78].

Nonetheless, it is imperative to acknowledge that the ICP algorithm possesses certain limitations. Noise points must be eliminated, such as point pairs with excessive distances or point pairs containing boundary points. Furthermore, alignment based on point pairs does not encompass local shape information, and determining the closest point in each iteration can be time-consuming. Given that this is a local minimization method, it relies on sufficient mutual overlap and adequate initial alignment of the two scans to be matched [62,79,80].

To address these limitations, several algorithms have been proposed that provide satisfactory coarse alignment. This can be achieved by establishing global correspondences based on local feature descriptors, which describe the local geometry around a point in a 3D point cloud [81,82].

2.3 Additive Manufacturing

Additive Manufacturing (AM), commonly known as 3D printing, constitutes a production technology that has brought about a profound revolution across various industrial sectors [83]. Originally conceived as a rapid prototyping method, AM is gradually evolving into a technique for producing finished component. In contrast to conventional material removal processes, often achieved through tools like Computerized Numerical Control (CNC) machines, AM creates products by progressively adding material layer by layer, eliminating the need for custom tooling and fixtures specific to each part. This technology embodies the potential for direct digital manufacturing, where products featuring intricate shapes or geometries are digitally represented in 3D model files and then divided into successive cross-sections to initiate the AM production process [84].

This manufacturing approach unveils a serveral advantages, including the capability to create highly intricate geometries that would be challenging or even impossible to achieve using conventional methods.

AM technologies differ in the processes used to create 3D objects layer by layer and each technology has its own characteristics, advantages and limitations, and is selected based on the desired material, specific applications and precision requirements. From the ISO/ASTM 52900:2021 International Standard, which provides a foundational grasp of the core concepts behind AM processes and offers concise explanations for the terminology and naming conventions used, it is possible to see as follows.

Among the primary technologies, within the Material Extrusion (MEX) processes, it is possible to identify the Fused Deposition Modelling (FDM) [85], which is also one of the most prevalent 3D printing techniques. This process involves the use of a thermoplastic filament that is melted and deposited layer by layer to construct the object. FDM printers find extensive use in rapid prototyping and the manufacturing of plastic components. Another prominent set of technologies includes Laser Sintering (LS) [86,87]. These procedures employ a laser to selectively melt or sinter metal or non-metal powder layer by layer, thereby producing solid objects. SLM is renowned for its capability to manufacture high-strength metal components, whereas SLS is versatile and compatible with a wide range of materials, including polymers and ceramics. Stereolithography (SLA) [88] stands as another noteworthy technology, wherein an ultraviolet laser progressively solidifies a layer of liquid photosensitive resin until the desired object is formed. SLA is valued for its precision and proficiency in creating intricate models. PolyJet [89], a technology akin to SLA, utilises jets of photocuring liquid resin that harden under UV light to fabricate objects. A distinctive feature of PolyJet is its ability to incorporate different types of plastics within the same object. Binder Jetting [90] is a process whereby a layer of powder is bonded together by a binder, typically a liquid adhesive, one layer at a time. This method is commonly employed for the production of coloured models and sand-based objects. Electron Beam Melting (EBM) [91] technology, akin to SL but using an electron beam instead of a laser, is renowned for its capacity to produce high-strength metal components. Laminated Object Manufacturing (LOM) [92] employs layers of material, often paper or plastic, which are cut and adhered together to form the final object. LOM is well-suited for the production of larger models and prototypes. Lastly, Directed Energy Deposition (DED) [93] is a process in which a nozzle deposits material in the form of powder or wire, while an energy source (such as a laser or electron beam) melts it to create the object. This technology is frequently utilised for the repair and production of large metal components.

2.4 Reverse Engineering

Engineering encompasses the entire life cycle of products and systems, involving their conception, manufacturing, assembly, and ongoing maintenance. Within the field of engineering, two distinct methodologies emerge: forward engineering and reverse engineering [94].

Forward engineering represents the conventional approach, progressing from high-level abstractions and logical designs towards the concrete realization of a system. However, in certain situations, there may be physical components or products that lack technical details such as drawings, bills of materials, or any form of engineering data. In these cases, the process of replicating an existing part, subsystem, or product, without drawings, documentation, or a computer model, is known as *reverse engineering* [95].

While the origins of reverse engineering theories and methodologies can be traced back to the 1980s, they initially gained prominence within the realms of software, hardware, and biological systems. However, the utility of reverse engineering techniques extends across various domains [96–99].

2.4.1 Overview

Reverse engineering has been defined in several ways, e.g., *“the method of formulating a comprehensive set of specifications for a complex hardware system through a methodical analysis of samples of that system”*[100] *or “the process of analysing a subject system to identify the systems components and their relationships, and to create representations of the system in another form or at a higher level of abstraction”* (Chikofsky and Cross [101]). In industrial engineering and in particular in mechanical design, reverse engineering may be described as the process that *“initiates the redesign process wherein a product is predicted, observed, disassembled, analyzed, tested, ‘experienced’, and documented in terms of its functionality, form, physical principles, manufacturability, and assemblability”* [102]. It has been regarded as a means to comprehend the functionality of a product [103], involving the replication of an item to create a surrogate model or clone for performance enhancement, as well as the extraction and application of embedded knowledge in novel designs. The focus on the geometric attributes of the product has driven substantial research growth in the field known as *Geometric Reverse Engineering* [12]. The predominant method for geometric reverse engineering involves extracting geometry from an existing product to reconstruct a 3D CAD model.

2.4.2 Process Phases

While multiple descriptions of the geometric reverse engineering process exist, they can all be summarised into three primary steps [104]:

1. Product digitization
2. Shape reconstruction
3. 3D CAD modelling.

Product digitization, in general, pertains to the process of converting a physical product into a digital format using measurement and scanning devices. This concept can encompass various other procedures that contribute to defining a virtual product or its characteristics, including mechanical simulation, manufacturing process simulation, and shape and topology optimization. Consequently, geometric reverse engineering doesn't solely concentrate on shape reconstruction from measurements but also emphasises the incorporation of material properties, manufacturing processes, and their inherent variations.

The process of shape reconstruction involves the determination of a surface that closely approximates an unknown shape based on collected samples. This is a challenging task because there can be multiple surfaces that approximate the given samples, and the point set may exhibit varying density, as well as noise and outliers due to the data acquisition process. The primary challenge here lies in ensuring the preservation of the original surface's topology, while accurately reproducing sharp features and surface boundaries in the reconstructed surface. The research literature offers a wide array of techniques to address these challenges. Initially, techniques using Non-Uniform Rational Basis Splines (NURBS) [105] or B-Splines [106] were employed to fit and combine local surface patches. However, these approaches revealed limitations when dealing with intricate physical objects, extensive data sets, sparsity, and noise. Furthermore, they are not suitable when considering physical properties such as material or object density.

The last stage in the process is 3D CAD modelling, where a geometric (solid) product model is crafted using either a Boundary Representation (B-Rep) or a feature-based parametric representation. This approach incorporates design intentions through geometric features, parameters, and constraints. Feature-based parametric models are frequently necessary for tasks like model inquiry, examination, or design alterations. Furthermore, they facilitate the development of Knowledge-Based Reverse Engineering (KBRE) methodologies, which can incorporate additional a priori information to overcome challenges such as incomplete or noisy data and to extract more comprehensive design and manufacturing data [107,108].

2.4.3 Geometric Reverse Engineering applications

Geometric reverse engineering is a pivotal process, especially for manufacturing companies seeking innovation in their product development. Indeed, in the manufacturing sector, specifically in generating production and quality assurance data for existing parts, this process involves the use of CAD models of prototypes for mold design and inspection automation, particularly for components with complex surfaces. In particular, industries such as aerospace, automotive, and biomedical prioritise the supply of intricate, high-quality components that adhere to stringent quality standards as a fundamental business objective [28,109–112]. With the widespread use of 3D solid models boasting precise engineering specifications, obtaining swift and precise results concerning any deviations from the design has become imperative. As the part-manufacturing process may not always accurately replicate a computer model, it is critical to identify where and to what extent the final product deviates from the intended design [113–121]. To achieve this, 3D scan data of production parts is compared to the original model through a process known as *deviation analysis* (chapter 2.5). This ensures that critical tolerances and quality standards are met. In the past, the sole available system for control was the Coordinate Measuring Machine (CMM), comprising a table and gantry that move along three axes, with a measuring head affixed at the end. While these machines boast high precision, the measurement process is slow as individual data points are acquired [122]. However, the advent of 3D acquisition tools has enabled rapid and thorough inspection of manufactured parts. This offers a comprehensive insight into geometry deviations, facilitating informed decisions or corrective actions.

In the medical field, geometric Reverse Engineering, referring to the process of 3D reconstruction, plays a pivotal role in bone and tissue reconstruction, benefiting patients afflicted by various conditions such as bone diseases, cancer, congenital defects, and traumatic injuries. Non-invasive scans like CT or Magnetic Resonance Imaging (MRI) provide data utilised to craft precise 3D models of implants and prostheses, especially thanks to AM technology, ensuring a perfect fit and integration into the patient's body. In the related field of dentistry, reverse engineering is making significant strides [123]. Specialised scanners and scanning software are employed to create digital dental impression models for diverse patient requirements.

In the realm of cultural heritage, the term “Virtual Heritage” [124] pertains to the process of digitally capturing the shape of artefacts for archaeological and historical purposes. Over time, physical artefacts deteriorate due to various factors, necessitating their preservation in virtual or replica form. Geometric Reverse Engineering method serves as a valuable tool in achieving this objective, enabling the creation of complete, 3D, durable, and unalterable digital archives. These archives can also serve as references for monitoring deterioration and planning restoration interventions. In this context, a notable project is the “Digital Michelangelo” [27] initiative, led by Stanford University, which digitised the renowned sculpture “David” in Florence, Italy. This digital model enabled experts to do examinations from unique perspectives, leading to discussions about Michelangelo's artistic intentions.

2.5 Geometric deviation analysis

As noted in the preceding paragraph, one of the principal domains of application for geometric reverse engineering lies in quality control for an object produced via traditional techniques or additive manufacturing. In this thesis, quality control is considered as the assessment of the level to which the produced component conforms to the virtual reference model. This assessment is carried out through a process termed deviation analysis, or more precisely, geometric (or shape) deviation analysis.

2.5.1 Data pre-processing

As previously mentioned, geometric reverse engineering techniques employ various acquisition methods to digitise a physical component. The primary outcome of these acquisitions, representing the rawest data obtained, consists of a point cloud. Various processing options are available for these point clouds, contingent upon the particular application. These options encompass the elimination of noise stemming from imperfect acquisition or background (typically unavoidable), downsampling, and surface extraction via point triangulation techniques, such as the Delaunay method. Once the representation of the physical component in the form of a point cloud is acquired, the registration process assumes a pivotal role in conducting deviation analysis. As expounded upon in chapter 2.2.3, registration becomes imperative to generate a unified point cloud by superimposing multiple views of the component, especially when acquisition methods fail to yield it through a single acquisition. Frequently, this recording process is already executed by the software connected to the acquisition tool. In the context of deviation analysis for quality control, the registration process is applied to the two point clouds: the one resulting from the digitization of the physical piece, which will be designate as the "target," and that of the reference model (termed the "model"), often obtained by extracting points coordinates from a Standard Triangulation Language (STL) model. In an ideal scenario, the two point clouds should exhibit perfect overlapping after the registration process. Nevertheless, in practice, this never occurs for a variety of reasons.

Primarily, the number of points in the two point clouds generally differs. Despite the availability of dedicated software tools for controlling the number of points to be incorporated into the model point cloud (whether increasing or decreasing them) and the number of points in the target point cloud (via the aforementioned downsampling techniques), a perfect overlap of points in the two point clouds is unattainable.

Additionally, apart from disparities in the number of points, which influence the overall density of the point clouds, it is imperative to acknowledge that local densities can vary significantly, particularly within the target point cloud. For instance, when employing a 3D scanner, certain regions on the surface of the physical object may undergo multiple scans, thereby resulting in a greater number of points in those specific areas. Conversely, due to the intricate geometry of the object, there will be regions that prove challenging, if not impossible, to scan, such as inlets or portions that partially overlap. These areas that are challenging to acquire result in holes[4] within the point cloud.

Furthermore, and even more relevant for quality control, the manufactured component may deviate from the shape of the initial model due to issues (some controllable, others less so) that arise during the manufacturing process.

2.5.2 Distances evaluation

Once the registration process is completed, through which a single point cloud is obtained where the model and the target are merged together, we then proceed with the actual geometric deviation analysis. The concept underlying the deviation analysis is quite straightforward: what is done is to evaluate the Euclidean distance between the points of the target and the model or vice versa. This distance can be assessed in two different ways:

---

[4] Areas within the point cloud where the presence of points would be expected but, instead, appear empty or devoid of data.

1. Point-to-point
2. Point-to-surface.

With the point-to-point distance, the aim is to assess, for each point of the target, its distance from the nearest point on the model. In the point-to-surface distance, the distance between each point of the target and the surface[5] of the model is calculated Although a generic distance, from a purely physical perspective, cannot be represented as a negative number, in this context, a sign is associated with the distance.

The data obtained from the computation of these distances are primarily evaluated for their mean and standard deviation. Another use of this data, highly valuable in the field of quality control, is the ability to associate a representative colour for deviation with each point on the target. In this way, it is possible to have a graphical representation of areas with greater deviation, and, in cases where distances have been calculated using the point-to-surface method, a judicious choice of the colour scale to use makes it evident which are the areas with over-material and which with under-material. The mean and standard deviation values obtained through the deviation analysis are subsequently employed to comprehensively assess the product's quality in relation to the fidelity of the piece's geometry compared to that of the reference model.

Ideally, when dealing with two perfectly overlapping point clouds, it is evident that both the mean and the standard deviation should equate to zero.

2.5.3 Issues and Limitations

Despite this procedure for conducting geometric deviation analysis being widely used, as evidenced by research in the scientific literature, it does have some limitations that can lead to incorrect interpretations of the results.

---

[5] It requires processing of the point cloud to extract its interpolating or approximating surface points.

The primary limitation arises from the fact that the Euclidean distance used to assess the distance between points in two point clouds does not possess commutative properties [125]. For example, within a deviation analysis, calculating the distance between each point in the target and the nearest corresponding point in the model, and then considering the reverse scenario, i.e., calculating the distance between each point in the model and the nearest point in the target, results in different outcomes. This discrepancy occurs due to differences in the number of points between the two point clouds, and even if the number of points were the same, the values obtained would not coincide. The difference in the number and values of distances becomes even more pronounced under specific conditions often encountered in practice. These conditions include variations in global and local densities, the presence of noise or points belonging to the background, and the existence of empty spaces.

All of these factors mean that the values of the mean and standard deviation are not representative and often divergent when assessing the quality of the object, leading to erroneous interpretations.

To address these issues, several precautions are typically taken. When working with point clouds of different densities, it is good practice to select the denser point cloud as the model and the less dense one as the target. When noise is present (which ideally should have already been removed through denoising) or empty spaces, i.e., partial overlap between the two point clouds, it is advisable to choose the less extensive point cloud as the target. In other words, one should select the point cloud that is free of noise or background or that contains empty spaces. All of these precautions can be applied if only one of the two point clouds exhibits these undesirable characteristics, and if it is known in advance which of the two is affected by them.

2.6 *Differential Entropy-based analysis*

2.6.1 *Differential Entropy*

Differential entropy represents a concept of significant relevance in both information theory and probability theory. It is the entropy of a continuous random variable and serves as a quantitative measure of the information contained within the variable itself. The origin of this concept dates back to 1948 when Claude Shannon introduced it in his article titled *"A Mathematical Theory of Communication"* [126]. This concept is sometimes referred to as Shannon entropy and is predominantly applied to discrete random variables.

The Shannon entropy, denoted as $H(X)$, of a discrete random variable X with a probability distribution $p(x)$, is defined by the following expression:

$$H(X) = -\sum_{i} p(x_i)\ \log_b(p(x_i)) \tag{8}$$

Where:

- $p(x_i)$ is the probability that the discrete random variable X takes on the value x_i, and the sum is performed over all possible values of x_i.
- b is the radix of the logarithm.

Given the frequent use of bits in computer science for encoding, it is a prevalent convention to employ the base 2 logarithm. As a result, differential entropy is quantified in bits, whereas the use of the natural logarithm introduces the *nat* unit of measurement, as initially exposed by Shannon.

For continuous probability distributions, Shannon entropy assumes the following form [127]:

$$H(X) = -\int_{-\infty}^{+\infty} f(x_i) \log_b(f(x_i)) \tag{9}$$

Where $f(x_i)$ is the Probability Density Function (PDF).

For each type of distribution employed, the expression for differential entropy varies. For instance, the differential entropy (expressed in nats) for a multivariate Normal distribution is:

$$h(X) = \frac{1}{2}\ln[(2\pi e)^{N} det\sum] \quad (10)$$

Where:

- N is the dimensionality of the data
- $\sum$ is the covariance matrix.

$\sum$ is a square matrix, symmetric and positive semi-definite which contains, in its main diagonal, the variances. Trought the use of $\sum$ it is possible to generalise the concept of variance to multiple dimensions.

The utilisation of the determinant of the covariance matrix ($det\sum$), also referred to as the *"generalised variance"*, was introduced by Wilks [128] as *"a scalar measure of overall multidimensional dispersion"* [129].

The applications of differential entropy are extensive and encompass several areas. In the field of information theory, differential entropy is employed to quantify the uncertainty or randomness associated with random variables, both continuous and discrete. The greater the entropy, the higher the degree of uncertainty associated with the random variable. In the context of data compression, it is utilised to determine the minimum number of bits required to efficiently represent a random variable. A notable example is Shannon coding, which is grounded in entropy theory. Differential entropy is also used in machine learning algorithms to assess the purity of a dataset, for instance, in decision trees-based methods. Minimising differential entropy enhances the algorithm's ability to learn more accurate predictions. Differential entropy also proves to be exceptionally valuable in the analysis of point clouds, particularly when examining the structure and randomness of data.

Point Clouds differential entropy

In the context of point clouds analysis, the process commences with data representation, treating the point cloud as a discrete probability distribution, and assigning each point a probability based on its frequency or density. This representation allows for each point to be regarded as a potential outcome of a random variable. Subsequently, the differential entropy formula is calculated. This computation aims to quantify the information and uncertainty inherent in the data. The computed entropy can be interpreted within the specific context of the application. A low entropy value typically indicates the presence of structure or a concentration of points in specific regions of space, suggesting that the data follows a certain order. Conversely, a high entropy value indicates greater randomness and dispersion of points in space.

2.6.2 CorAl Method

Overview

Drawing inspiration from the research of Droeschel and Behnke [130], Adolfsson et al. [131,132] introduced a novel approach: "*Are the point clouds Correctly Aligned?*" (*CorAl*). CorAl, grounded in the principles of differential entropy, provides a means to evaluate the precision of point clouds registration. The fundamental premise of this methodology lies in the idea that in cases where two point clouds are well-aligned, the entropy of their joint point cloud (union of the two point clouds) should not exhibit an increase in comparison to the sum of the entropies calculated individually for each of the two point clouds. Conversely, when minor misalignments are present between two point clouds, the joint entropy tends to increase. Consequently, the CorAl method employs this form of measurement to identify subtle alignment errors and, by introducing a quality index denoted as Q, assess the alignment's overall quality.

Method explanation

Examining a point cloud P consisting of a collection of points in the 3D Cartesian space ($\mathbb{R}^3$) $p_i = [x\ y\ z]$. CorAl calculates the differential entropy h_i for every point in P, in accordance with Eq. 5:

$$h_i(p_k) = \frac{1}{2} ln[(2\pi e)^N det\sum(p_k)] \tag{11}$$

Where:

- $N = 3$ (Dimensionality of the data)
- k is the count of points located within a neighbourhood (ρ) defined by a radius r (assuming it to be circular) and cantered around each p_i
- $det\sum(p_k)$ is the determinant of the sample covariance matrix calculated based on the points p_k located within the neighbourhood of P_i
- p_k is the set of k-points within the neighbourhood.

The total differential entropy H of the point cloud P is obtained by summing the evaluated h_i values for each point:

$$H(P) = \sum_{i=1}^{|P|} h_i(p_k) \tag{12}$$

Where $|P|$ is the number of points in P.

When dealing with two point clouds, P_A and P_B, it is feasible to compute their separate entropy (H_{sep}) as well as their joint (H_J) average differential entropy:

$$H_{sep} = \frac{H(P_A) + H(P_B)}{|P_A| + |P_B|} \tag{13}$$

$$H_J = \frac{H(P_{joint})}{|P_{joint}|} = \frac{H(P_A \cup P_B)}{|P_A| + |P_B|} \tag{14}$$

Where:

- P_{joint} is the joint point cloud $(P_A \cup P_B)$
- $|P_{joint}|$ is the number of points in P_{joint}.

The alignment quality measure Q is subsequently derived using the following formula:

$$Q(P_A, P_B) = H_J - H_{sep} \tag{15}$$

It is also viable to assess the quality index on a per-point basis. This per-point index q_i enables the generation of a graphical representation depicting the misalignment of the points:

$$q_i(p_k) = [h_i(p_k)]_{joint} - [h_i(p_k)]_{sep} \tag{16}$$

The CorAl method is thus capable of assessing the quality of the registration of two point clouds by identifying discrepancies arising from both rigid misalignments and distortions that may occur during scanning, such as during a LiDAR scan in motion.

3 MATERIALS AND METHODS

3.1 Novelties overview

The key innovations introduced in this thesis are based on the analysis of point clouds using differential entropy (chapter 2.6) and can be summarised as follows:

1. Modification of the differential entropy formula for multivariate and univariate Gaussian distributions. (chapter 3.2)

2. New method for quality control through geometric deviation analysis. (chapter 3.3)
3. Introduction of a compactness index for the analysis and description of systems representable by point clouds. (chapter 3.4).

It's worth noting that all the calculations and graphs were generated using Matlab [133].

3.2 Revised Differential Entropy Formulation

The investigation into the differential entropy of point clouds, undertaken to formulate this thesis, has highlighted certain distinctive aspects of the methodology, which have been meticulously examined.

3.2.1 Determinant Study

In the formula (Equation 11) utilised for computing the differential entropy, the generalised variance ($det\sum$) is a prominent factor. Assuming a 3D point cloud is considered, and the neighbourhood ρ for each point is evaluated, the study categorises four scenarios based on the number of points (k) present in the neighbourhood:

1. $k = 1$ → Only the point under examination exists in ρ, and $\sum$ assumes a real value equal to its determinant, signifying the variance, which is zero for a single point.
2. $k = 2$ → In ρ, there is only one additional point alongside the one under examination. As two points always fall on the same line, considering the diagonal form of $\sum$, it becomes evident that it possesses only one non-zero eigenvalue, indicating that the points are aligned on a straight line. Consequently, the determinant will be zero.

3. $k = 3$ →When three points in space are considered, and they are not aligned, they will invariably lie on the same plane. Therefore, by evaluating the eigenvalues of $\sum$, it becomes apparent that one of them will be zero, indicating a planar distribution of points. Once again, the determinant of $\sum$ will be zero.
4. $k > 3$ → When the number of points exceeds 3 and they are non-coplanar, all eigenvalues and the determinant of $\sum$ will be non-zero.

3.2.2 Differential Entropy: negative values

Depending on the arrangement of the points, the utilisation of Equation 11 can yield negative entropy values, a scenario that arises when the argument of the logarithm is less than 1. Given the objectives of the applications put forth in this thesis, such as the analysis of geometric deviation and the introduction of the compactness index, efforts were made to mitigate this effect. As the contributions stemming from Equation 11 combine to determine the overall entropy of the point cloud, an adjustment was implemented to this equation, guided by the principles outlined in Equation 12. The primary goal was to standardise the entropic contributions of each point, making them comparable in magnitude and sign. This standardisation was essential to prevent potential compensation effects stemming from the simultaneous presence of both positive and negative values.

This adaptation assumes particular significance in the context of deviation analysis. In cases where disparities exist between different point clouds, it becomes paramount that these disparities are equally weighted to derive an overarching index that accurately reflects the quality of the production part. Similarly, in the introduction of a compactness index, each point's significance is pivotal, especially concerning the proposed applications, as detailed in 3.4.

3.2.3 Modified differential entropy formula for a normal multivariate distribution

The modification to the differential entropy is the following:

$$h_i(p_k) = \frac{1}{2}\ln[(2\pi e)^N det\sum(p_k) + 1] \tag{17}$$

The inclusion of the term $(+1)$ in the formula effectively resolves both the issues associated with the null determinant of $\sum$ and those related to negative values of the differential entropy. Indeed, in all situations where the determinant is zero, the initial part of the logarithmic argument becomes null, and the addition of the value $(+1)$ yields a differential entropy result of zero. Consequently, in cases where the number of points is $k \leq 3$, the entropic contribution becomes zero.

Concerning a relatively dense point cloud, as typically obtained through scanning (such as in deviation analysis), the decision to "sacrifice" information in the presence of few points appears highly reasonable for two main reasons. First, it is exceedingly rare for a scanned point cloud (especially those generated using structured light scanners or confocal microscopy) to contain fewer than 4 points unless extremely small search radii with no practical significance are used. However, in cases where this situation does occur, it may be attributed to the presence of noise.

The second reason for adopting this modification to the formula is specifically tailored to address this condition. Noise, consisting of a few scattered and isolated points, should not contribute to the computation of the overall entropy of the point cloud. This feature proves particularly advantageous in the innovative applications introduced in this thesis: in the context of deviation analysis, noise would not adversely impact the quality index value, and in the context of a compactness index, a point sufficiently distant from others would not hold significance.

3.3 DEDA – “Differential Entropy for Deviation Analysis

In this chapter, a novel method named "Differential Entropy for Deviation Analysis" (*DEDA*) is introduced. This method was developed during the course of this thesis and is based on the CorAl method, as previously described in chapter 2.6.2. As mentioned earlier, CorAl is a method that leverages the differential entropy of point clouds to assess the alignment between two sets of points obtained from LiDAR sensors, using a quality index denoted as Q. The adjustments made to Equation 11 of differential entropy and the considerations outlined in chapter 3.2.1 led to the inception of *DEDA*. This innovative method is structured as a robust approach for the analysis of geometric deviations, particularly within the context of quality control for components produced using traditional or AM techniques. Furthermore, the method proposed in this thesis aims to address many of the limitations inherent in traditional methods, which are predominantly reliant on Euclidean distance calculations.

3.3.1 Method

The procedure behind *DEDA* is analogous to that of CorAl, as previously mentioned. Essentially, it involves the following steps: calculating the entropy of the two point clouds separately, calculating the entropy of the combined point cloud, and evaluating the difference between the entropy of the second and the first point cloud to obtain the quality index.

The main differences are found in the modification of the differential entropy formula, using Equation 17 instead of Equation 11, as previously mentioned. This modification automatically permits the consideration of a null entropic contribution for the points that, in their neighbourhoods, encompass from one (themselves) to three points. This occurs because in 3D space, when the value of k is less than or equal to 3, the determinant of the covariance matrix becomes zero and, adding the 1, will result in $h = 0$. Consequently, neighbourhoods with a limited number of points do not impact the calculation of the total entropy of the point cloud. This allows the exclusion of potential noise when evaluating the differential entropy of the acquired point cloud. It is important to note that in dense point clouds obtained through techniques such as structured light, the use of an appropriate value for the radius r ensures that the number of points within each neighbourhood far exceeds 3. Consequently, excluding these points has no effect on the calculation of the total differential entropy of the point cloud. Furthermore, in all other cases where the value of $k \geq 4$, modifying the formula ensures that the logarithm argument is always greater than 1, resulting in a logarithm that is consistently greater than 0. This implies that the entropy h_i will always be positive, in contrast to what occurs with Equation 11.

In summary, it can be stated:

$$h_i(p_k) = \begin{cases} 0 & if \quad 1 \leq k \leq 3 \\ a \in \mathbb{R}: a > 0 & if \quad k \geq 4 \end{cases} \tag{18}$$

Figure 2 schematically depicts the flowchart of the *DEDA* method.

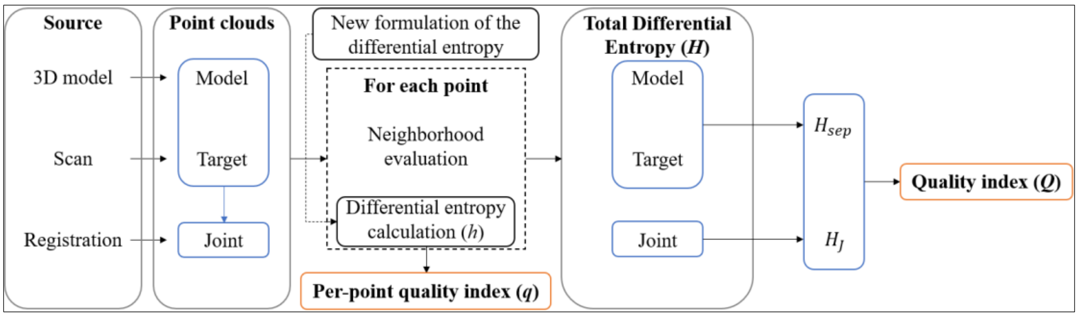

Figure 2. Flowchart of the *DEDA* method.

3.3.2 Application

For the application of the *DEDA* method, the choice was made to conduct geometric deviation analysis on objects produced using AM, specifically with FDM technology. The selected model is the Stanford Bunny (**Figure 3**), originally developed by Turk and Levoy [134].

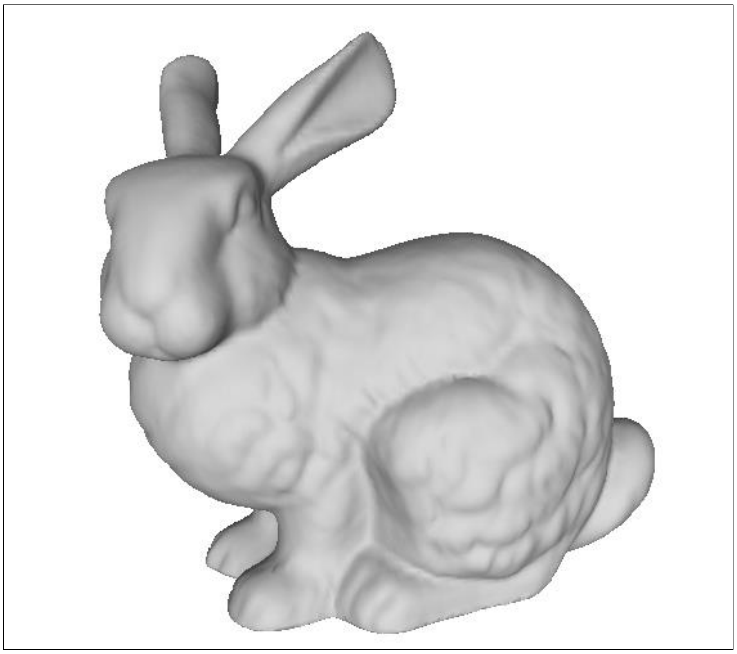

Figure 3. Stanford Bunny model.

This model is widely employed in scientific literature for similar applications. The fundamental approach involved printing samples of varying known qualities and subsequently performing deviation analyses using the *DEDA* method to verify whether the quality index accurately reflected the expected print quality.

Additionally, a robustness analysis of the *DEDA* method was carried out to highlight its capability to address various limitations often encountered by classical methods. This analysis pertained to evaluating the *DEDA* method's performance in scenarios involving the presence of holes, noise, or background in the point cloud, as well as variations in point density between the two compared point clouds.

Data preparation

To simulate different print qualities, three Bunny objects were created with varying layer thicknesses[6]: 0.15 mm, 0.25 mm, and 0.32 mm. All other printing parameters remained unchanged and are detailed in **Table 1**.

---

[6] There is therefore an increase in quality as the thickness of the layer decreases.

Table 1. Printing parameters.

Parameter	**Value**
Nozzle diameter	0.4 mm
Nozzle temperature	200 °C
Bed temperature	60 °C
Printing speed	50 mm s^{-1}
Printing infill	20 %

The objects were produced using the Creality Ender 6 3D printer (Creality 3D Technology Co, Shenzhen, China). It's important to note that no support structures were used during printing, and the objects were crafted from the same coil of PolyLactic Acid (PLA) filament, stored in a specialised dehumidifier to preserve its properties. Subsequent to printing, the three samples were rendered opaque using a specialised spray to enable 3D scanning. Scanning was performed with a structured blue light optical scanner (ATOS Compact Scan 2M by GOM) with a projector and stereo-camera system. The key characteristics of the scanner used are provided in **Table 2**.

Table 2. Characteristics of the 3D scanner.

Characteristic	**Value**
Camera position	300
Wavelength	400 – 500 nm
Scanner focal length	12 mm
Stereo camera focal length	17 mm
Stereo camera angle	25°
Stereo camera resolution	1624×1236 px 2,000,000 points per scan
Distance scanner – subject	570 mm
Measuring volume	250×190×190 mm
Point spacing	0.153 mm

Markers were employed during the scan and placed in close proximity to the object being scanned, aiding the scanner registration process to obtain a comprehensive point cloud of the object through multiple acquisitions from various views.

It is important to clarify that three scans were conducted for each Bunny, and all the numerical results presented refer to the mean values obtained.

After obtaining the point clouds, each of them was aligned with the original point cloud (model) using a two-phase registration process carried out with the CloudCompare software [135]. The initial phase involved identifying four pairs of corresponding points in the two point clouds (target and model) to establish an initial pre-alignment. Subsequently, the ICP algorithm was employed in a point-to-point configuration. As previously mentioned, given that the calculation of the Euclidean distance between two point clouds is not commutative, distances between target-model and model-target were assessed. For clarity in presentation, an identifying code (ID) was assigned to each point cloud and each comparison performed, as illustrated in **Table 3** and **Table 4**.

Table 3. Point clouds description.

Single point cloud	ID	No. points
Bunny original (model)	B0	31,994
Bunny 1 (0.15 mm)	B1	199,536
Bunny 2 (0.25 mm)	B2	201,548
Bunny 3 (0.32 mm)	B3	203,332

In addition, it is important to note that Bunny 1, Bunny 2, and Bunny 3 represent the samples obtained with different layer thicknesses, as indicated in parentheses.

Table 4. Joint point clouds for geometric deviation analysis.

Joint Point cloud	ID
B0 → B1	J1
B1 → B0	J1’
B0 → B2	J2
B2 → B0	J2’
B0 → B3	J3
B3 → B0	J3’

3.3.3 Results and Discussions

Geometric Deviation Analysis: classical method

The results of the deviation analysis, conducted by evaluating the Euclidean distance, are presented in **Table 5** in terms of the mean (μ) and standard deviation (σ).

Table 5. Results of geometric deviation analysis with classical method.

Joint Point cloud	**μ**	**σ**
J1	0.1660	0.0780
J1’	0.7659	2.0291
J2	0.1618	0.0823
J2’	0.5731	1.5515
J3	0.1638	0.0793
J3’	0.6487	1.7718

From **Table 3**, it is evident that B0 is less dense than the point clouds obtained from scanning. Therefore, to evaluate the distance, the less dense point cloud should be considered in comparison to the denser one. In this case, this condition is known a priori, so only the analyses related to J1, J2, and J3 will be considered reliable. The others are presented merely to demonstrate the non-commutativity of the Euclidean distance between two point clouds.

In the analysis of the mean and standard deviation values obtained for J1, J2, and J3, there emerges a lack of a clear distinction in the quality of the produced pieces. Typically, lower mean and standard deviation values indicate better quality. However, upon examining the average values, we notice that J2 has lower values than J3, while J3 has higher values than J1. This trend is not confirmed in the standard deviation values, as they are higher in J2 and lower in J1. Based solely on the average values, it would seem that the best quality should be attributed to J2 and the worst to J3. However, it's important to note that even though J3 exhibits the worst quality in terms of layer height, the best quality should be associated with J1 due to its lowest standard deviation. It's therefore worth noting that an analysis based solely on these two parameters doesn't provide a definitive conclusion regarding the quality of the produced piece.

Geometric Deviation Analysis: DEDA method

Subsequently, the *DEDA* method was employed, and it is considered to be applied to J1, J2, and J3 for simplicity since the issue of commutativity does not arise. In this phase, the influence of the search radius on the quality index Q was also assessed, leading to analyses at various neighbourhood sizes (r = 1.5, 2, 2.5, 3, 3.5 mm). Similar to the CorAl method, the *DEDA* method provides a global quality index (Q) and one relative to each point (q_i). The first is used to express the quality of the object in terms of geometric fidelity to the reference model qualitatively and unequivocally. The second, plotted with a colour scale, enables visualization of the areas of the produced piece that deviate the most from the model.

Table 6 displays the Q values obtained at varying search radii, while **Figure 4** graphically represents them, emphasizing the results of the deviation analyses conducted using the *DEDA* method.

Table 6. Q values at varying search radii.

Radius (mm)	**Q_{J1} (10^{-3})**	**Q_{J2} (10^{-3})**	**Q_{J3} (10^{-3})**
1.5	1.371	1.541	1.728
2	1.770	1.879	2.029
2.5	1.18	1.25	1.528
3	0.687	0.795	0.986
3.5	1.503	1.676	1.799

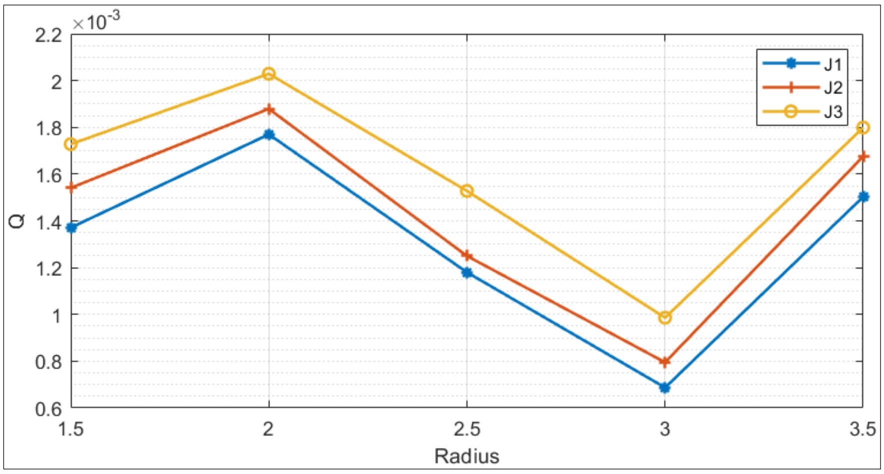

Figure 4. Q trends at varying search radii.

From the graphical representation, it is evident that the quality of the piece, measured using the Q index, is consistently distinguishable as the search radius varies. The closer the Q value is to zero, the better the alignment and, consequently, the fidelity to the model. Furthermore, as it is known a priori that J1 represents the best print quality and J3 the worst, it can be observed that, for each search radius, Q_{J1} is consistently the lowest, Q_{J3} consistently the highest, and Q_{J2} maintains an intermediate value. Therefore, the Q index evaluated using the DEDA method can uniquely and quantitatively assess the geometric deviation between the two point clouds.

Finally, it is possible to visualise the point cloud where points are color-coded based on q_i (per-point quality index) to obtain a graphical representation of the areas of the piece with the greatest deviation. As an example, **Figure 5** illustrates the comparison between J1 and J3, the samples with the best and worst quality.

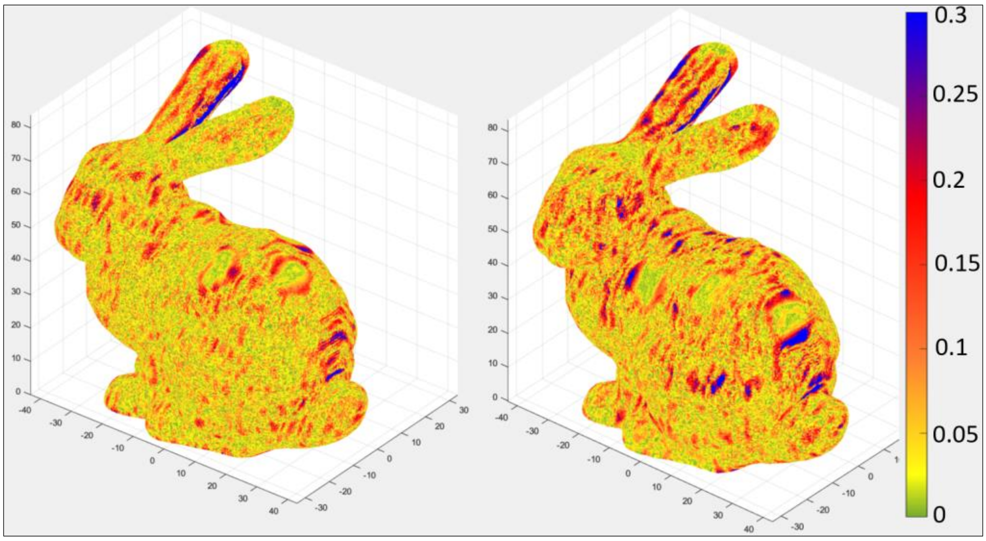

Figure 5. Comparison between J1(left) and J3(right), coloured with the per-point quality index.

Analysing the colormap, it's noticeable that in J3 (on the right), the areas with higher q values (indicating lower quality) are more extensive compared to J1.

DEDA Robustness assessment

In order to evaluate the method's reliability and emphasise the benefits that *DEDA* offers for quality control, three distinct point clouds were intentionally generated by altering B1. The initial scenario simulates the existence of holes in the scan, attributed to the scanner's inability to detect points in shaded regions caused by specific geometrical characteristics of the sample. The second scenario replicates the presence of extraneous points that do not represent the target geometry, arising from factors like inadvertent background capture, noise or the partial overlap in two point clouds. The third scenario emulates the comparison of point clouds with varying point densities. All of these conditions pose significant challenges in traditional deviation analysis. This is because, in cases where a point cloud lacks a direct correspondence with another, the deviation can be considerably influenced. Furthermore, it's worth noting that deviation analysis, based on Euclidean distances, does not possess a commutative property, as previously discussed.

Additionally, to establish a reference for comparing deviations resulting from the aforementioned issues and actual alignment challenges, two additional point clouds were generated from B1. These were achieved through a 1 mm translation along the x-axis and a 1-degree rotation around the barycentric z-axis. For this robustness analysis, the overlap of B1 with itself (denoted as RA0, representing the ideal scenario) and the overlap with the modified versions of B1 (RA1, RA2, RA3, RA4, and RA5) outlined in **Table 7** was taken into consideration. This analysis encompassed the utilization of both conventional deviation analysis and the implementation of the *DEDA* method.

Table 7. Joint point clouds for *DEDA* robustness assessment.

Joint point cloud	**ID**
B1 – B1	RA0
B1 – B1 External points	RA1
B1 – B1 holes	RA2
B1 – B1 50% downsampled	RA3
B1 – B1 translated	RA4
B1 – B1 rotated	RA5

The results of the deviation analysis for robustness assessment, conducted both with the classical method and with the *DEDA* method, are presented in **Table 8**.

Table 8. Results of robustness assessment (classical and *DEDA* methods).

ID	**μ (σ)**	**Q**
RA0	0 (0)	0
RA1	0.05 (0.89)	0
RA2	0.05 (0.40)	$1.70 \cdot 10^{-4}$
RA3	0.12 (0.15)	$9.30 \cdot 10^{-3}$
RA4	0.46 (0.28)	$1.36 \cdot 10^{-1}$
RA5	0.23 (0.12)	$3.18 \cdot 10^{-2}$

From **Table 8** the following considerations can be made.

As evident, the values of Q, μ, and σ are all zero for RA0. However, for RA1, the Q value also remains at zero, in contrast to the relative values derived from the classical analysis based on Euclidean distance. Comparatively, the Q values for RA2 and RA3, in comparison to those for RA4 and RA5, are notably lower by one or two orders of magnitude. Conversely, the values obtained from the classical analysis exhibit variations. Notably, while μ remains lower in RA2 and RA3 than in RA4 and RA5, σ values are either comparable or even higher in the former case. It is essential to note that, due to the non-commutative nature of the point cloud comparison (with classical methods), as previously done, deviation analysis was assessed in both directions, and the worst μ and σ values were considered. The decision to consider the worst conditions was based on the recognition that, unlike these artificially induced tests where issues were introduced into only one point cloud, real-world scenarios could typically affect both point clouds simultaneously.

Figure 6 displays point clouds, coloured with the q_i, pertaining to the tests conducted in the robustness assessment.

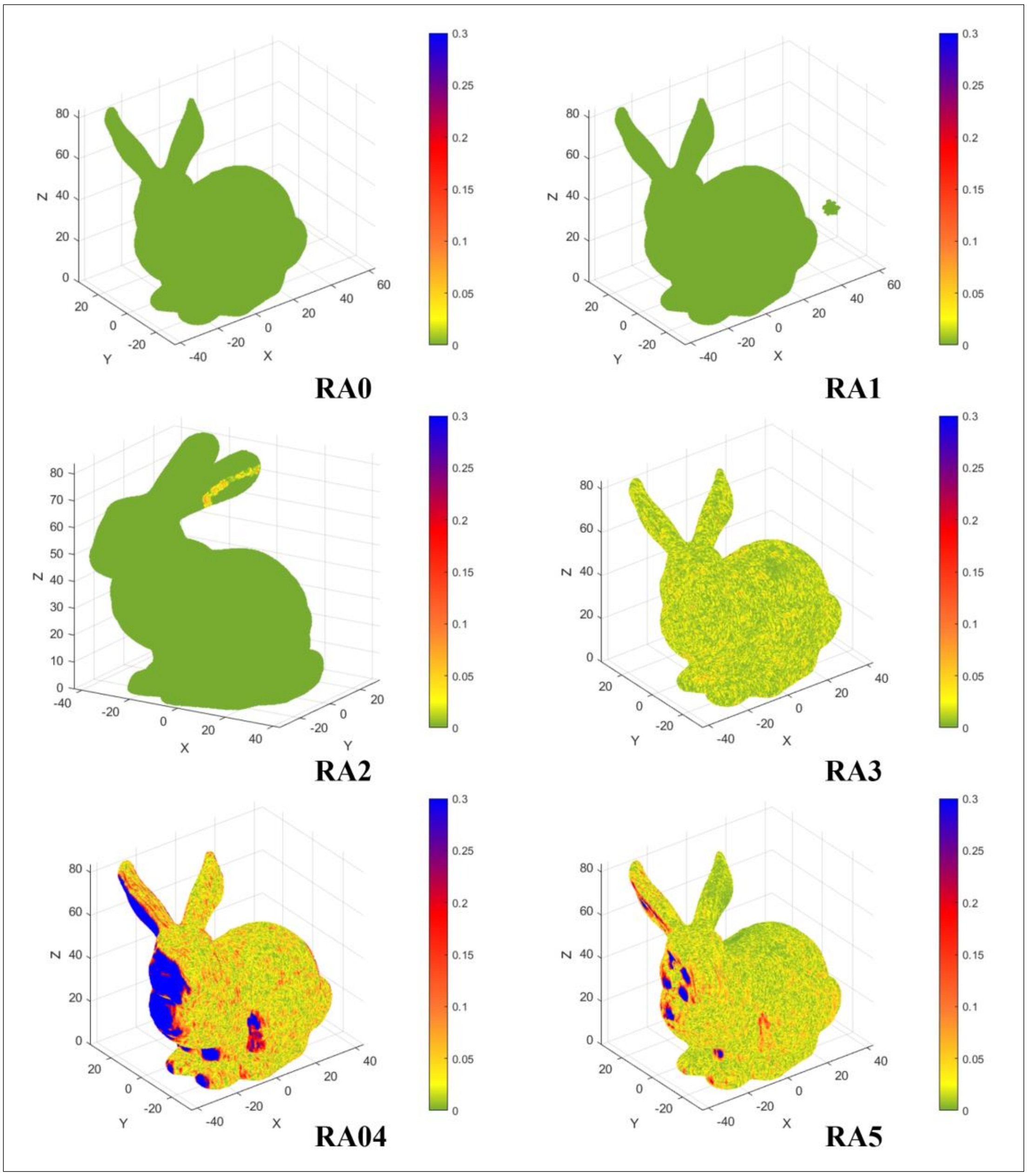

Figure 6. Point clouds coloured with the per-point quality index for the robustness assessment.

From **Figure 6**, it is evident that in RA0, as expected, the per-point quality index is zero in every area of the point cloud. This is also observed in RA1, where, despite the presence of points outside the point cloud, they are not computed in the deviation analysis using the *DEDA* method. In that area, since there are no points from the model point cloud, there is no difference between the entropy calculated in the individual point cloud and that calculated in the combined point cloud. Therefore, the terms in Equation 16 are equal, resulting in a q_i value of 0.

In RA2, the q value is zero over the entire point cloud, except in the interface areas between B1 and B1 holes. This occurs because the entropy varies in the joint point cloud due to the presence of a hole in the scan. The result is a slight edge effect, which becomes less pronounced with an increase in the search radius.

In RA3, a generalised increase in q values can already be observed, owing to the different point cloud densities. However, this increase is significantly less pronounced compared to real misalignments (RA4 and RA5). As indicated by the numerical data, the increase in Q in the presence of different point cloud densities is smaller than that observed in the presence of obvious misalignments, i.e., marked geometric differences between the two compared point clouds.

3.4 DECI – “Differential Entropy-based Compactness Index”

In this chapter, the "Differential Entropy-based Compactness Index" (*DECI*) will be introduced as an innovative metric, and its potential applications will be highlighted. This index, developed as a method for describing the spatial distribution of points, is believed to also provide a new approach to evaluate risk, congestion, and other aspects related to the representation of systems that can be schematised as point clouds.

The possible applications of this method are broad and range from maritime, air, and road traffic control (including autonomous driving) to crowd density monitoring in public and indoor spaces.

DECI could prove highly versatile in areas such as health, biology, and sports analytics, offering a broad spectrum of possible uses that merit further analysis and exploration.

3.4.1 Method

Given what has been already said, the *DECI* index has been defined as follows:

$$DECI_i(P_i) = \frac{\sum_1^n deci_i(p_k)}{n} \tag{19}$$

Where:

$$deci_i(p_k) = \begin{cases} 0 & if \quad h_i(p_k) = 0 \\ \frac{1}{h_i(p_k)} & if \quad h_i(p_k) \neq 0 \end{cases} \tag{20}$$

In this way, an index is obtained that takes on a zero value for sufficiently sparse points distributions and increases as points get closer to each other.

Figure 7 schematically illustrates the method used to obtain the *DECI*.

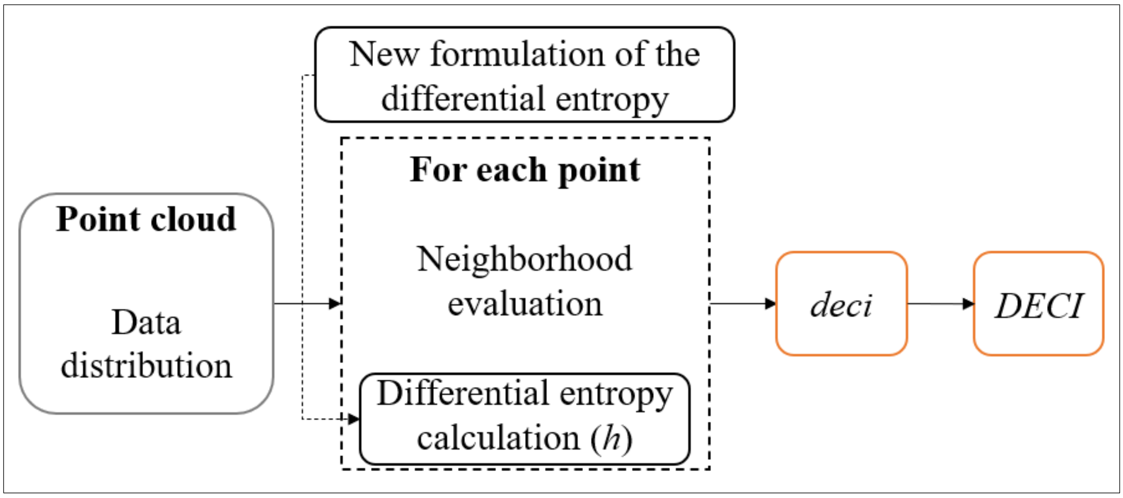

Figure 7. Flowchart of the *DECI***.**

3.4.2 Application

Based on the discussion in chapter 3.2.1 regarding the determinant of the covariance matrix, and for clarity in presentation, the following considerations can be made, assuming a 2D distribution:

$$k = 1 \rightarrow h_i = 0 \tag{21}$$

$$k = 2 \rightarrow h_i = \frac{1}{2}\ln[(2\pi e)^2 \, (\sigma_X + \sigma_Y)^2 + 1] \tag{22}$$

$$k \geq 3 \rightarrow h_i = \frac{1}{2}\ln[(2\pi e)^2 \det \sum + 1] \quad (23)$$

Where:

- σ_X and σ_Y are the variances on X-axis and Y-axis respectively.

In defining a compactness index, it is important that all points have their own weight if they interact with neighbouring points. Therefore, although an isolated point (Equation 21) has a zero influence since its entropic value, and consequently the value of the *deci* related to it, is also zero based on Equation 20, in the case where $k = 2$, it is not considered appropriate to bypass the calculation as done for deviation analysis. Therefore, in this condition, in which it is not possible to use $\det \sum$ (as it is null), another type of invariant was sought to replace it while maintaining its geometric meaning.

In fact, the determinant turns out to be an invariant, which means in practice that the entropy, and consequently the value of the compactness index, does not vary either with the rotation or with the translation of the point cloud. Another invariant that can be extracted from $\sum$ is its trace, given by the sum of the elements on its main diagonal, i.e., the sum of the variances in the two axes, X and Y. The square of this sum was inserted to standardise the units of measurement.

Application

An application of the method on a 2D random point cloud is now presented to analyse the application characteristics and potential of the *DECI* index. In particular, the variation of the *DECI* value is examined as the search radius (r) changes. The experiment analyses first a random 2D point cloud ($D1$) consisting of 100 points located within a 500×500 box with lower limits set at 0 and upper limits set at 500 on both axes (X and Y). The *DECI* of $D1$ was assessed by altering the radius (r) of the neighbourhood (radius values: 10, 20, 30, 40, 50, 60, 70, $+Inf$[7]).

Another scenario was assessed in which, again using the distribution of $D1$, a randomly varying search radius ($0 < r < 50$) was assigned to each point (p_n). No specific unit of measurement was employed, but it is important to note that this unit of measurement corresponds to the physical quantity of length.

Results and Discussions

The *D1* distribution was analysed with a uniform search radius applied to each data point.

Figure 8 illustrates the *deci* values for individual points and the resultant *DECI* value for the distribution when a search radius of 10 is utilised. In **Figure 9**, a specific area within the distribution is examined to elucidate the operation of the compactness index.

---

[7] Radius value $+Inf$ means a radius large enough to encompass all the points of the distribution.

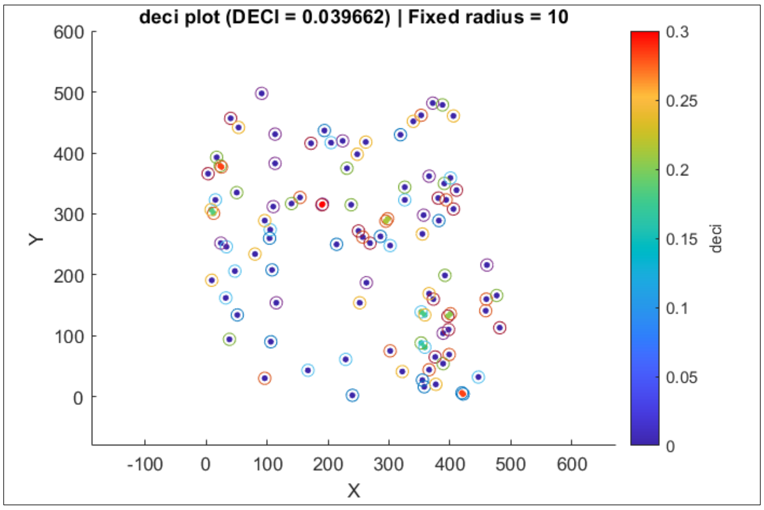

Figure 8. *DECI* and *deci* values for *D1* with a search radius of 10.

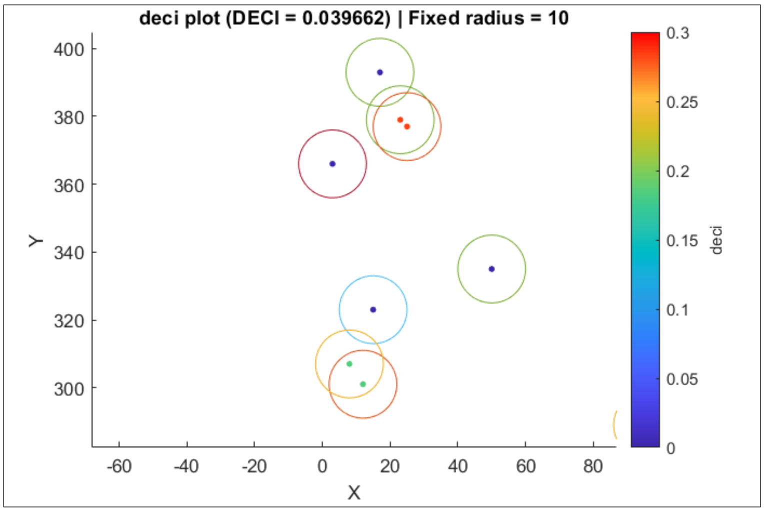

Figure 9. *Detail of D1* with a search radius of 10.

It is evident that points sufficiently distant from others exhibit deci values of 0. Moreover, in the instance of two pairs of points situated in close proximity, the deci value is greater for the upper pair compared to the lower pair.

Figure 10 and **Figure 11** show two examples of *D1* with different search radius values (20 and 30 respectively). An increase in *DECI* becomes evident.

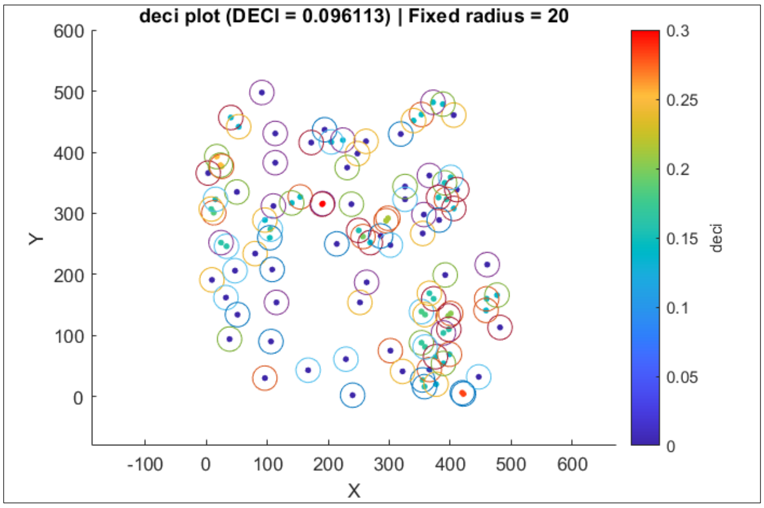

Figure 10. *DECI* and *deci* values for *D1* with a search radius of 20.

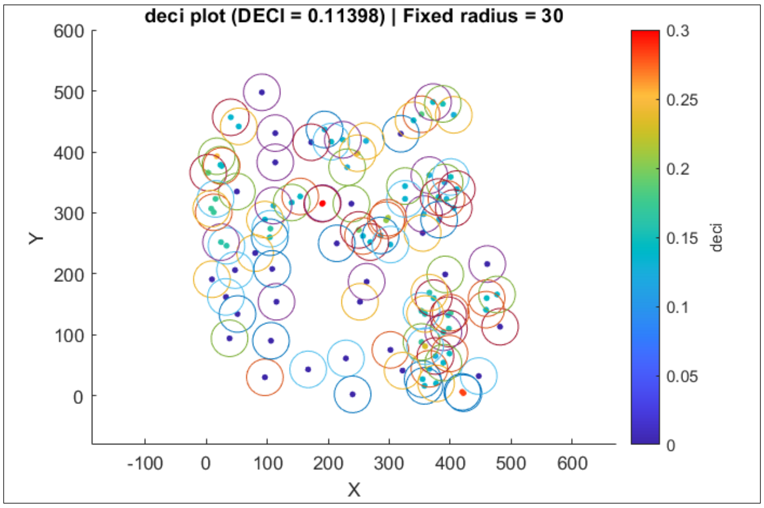

Figure 11. *DECI* and *deci* values for *D1* with a search radius of 30.

A particular of the distribution is shown in **Figure 12** and in **Figure 13**, in which is possible to see the behaviour of the *deci* as the radius increases (20 to 30).

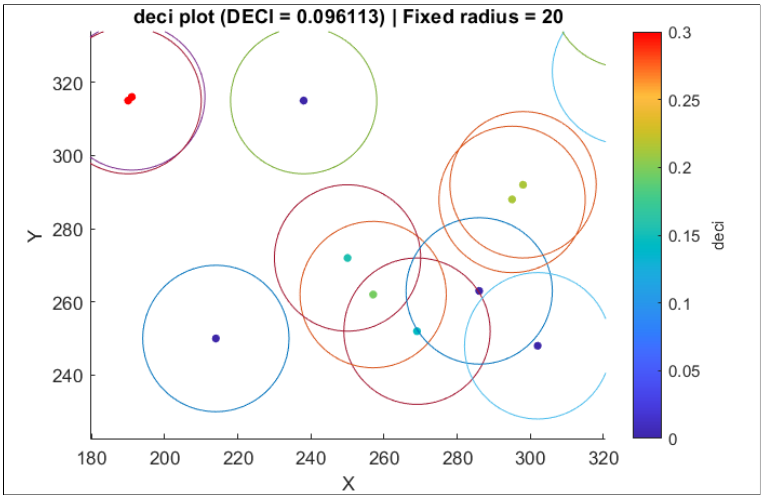

Figure 12. *Detail of D1* with a search radius of 20.

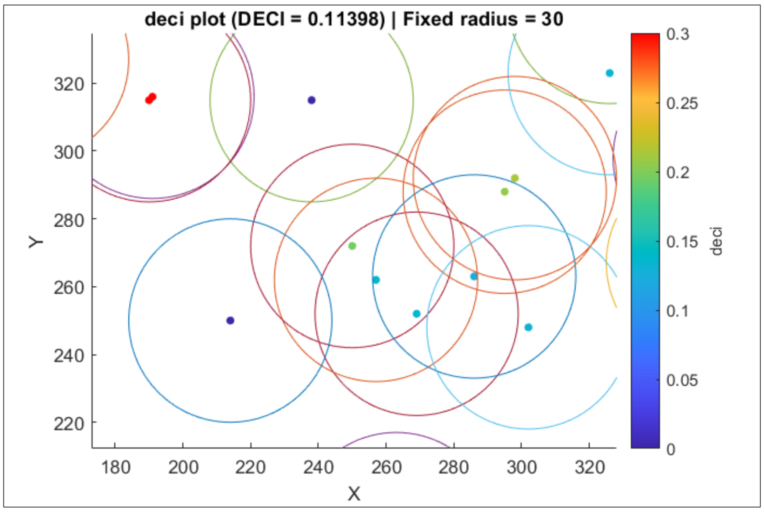

Figure 13. *Detail of D1* with a search radius of 30.

From the preceding images, variations in *deci* and *DECI* can be observed as the radius changes. An increase in *DECI* can already be noticed. **Figure 14**, **Figure 15**, **Figure 16**, and **Figure 17** depict the other cases with radius value equal to 40, 50, 60, and 70 respectively.

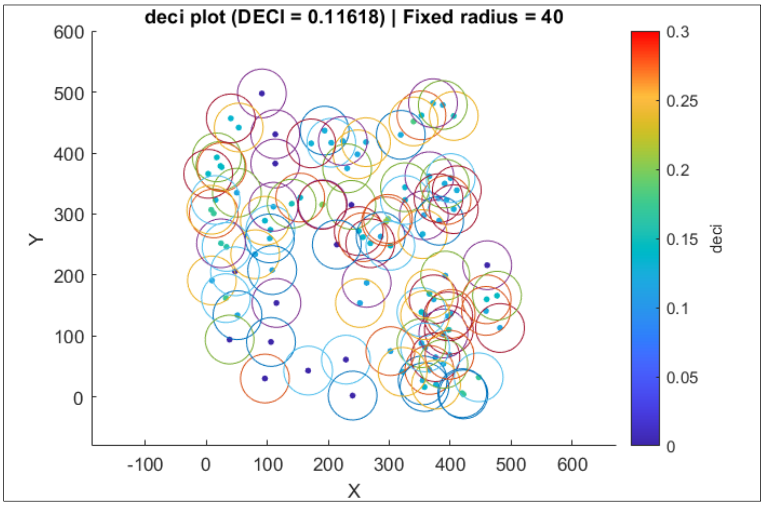

Figure 14. *DECI* and *deci* values for *D1* with a search radius of 40.

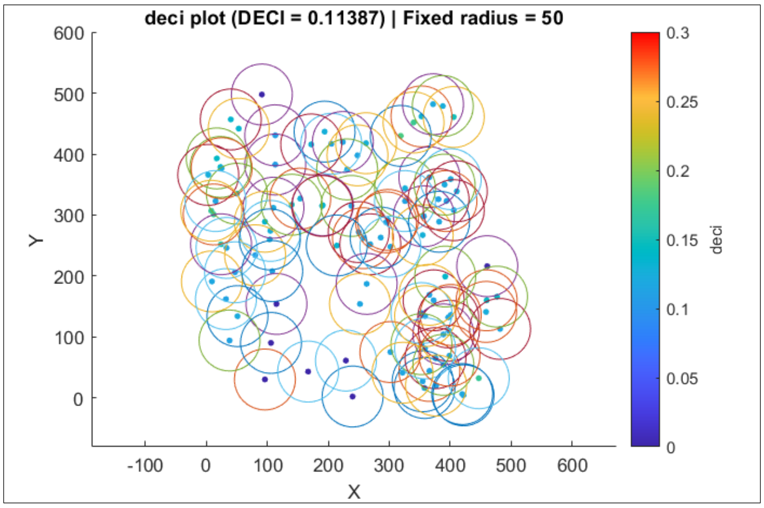

Figure 15. *DECI* and *deci* values for *D1* with a search radius of 50.

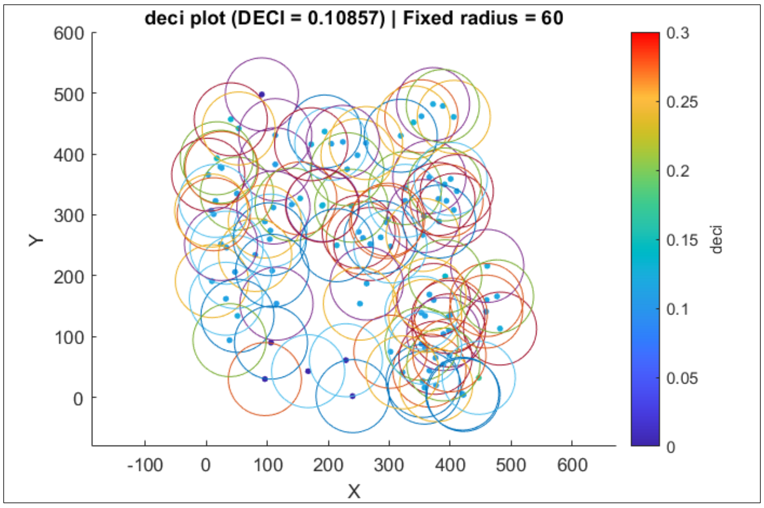

Figure 16. *DECI* and *deci* values for *D1* with a search radius of 60.

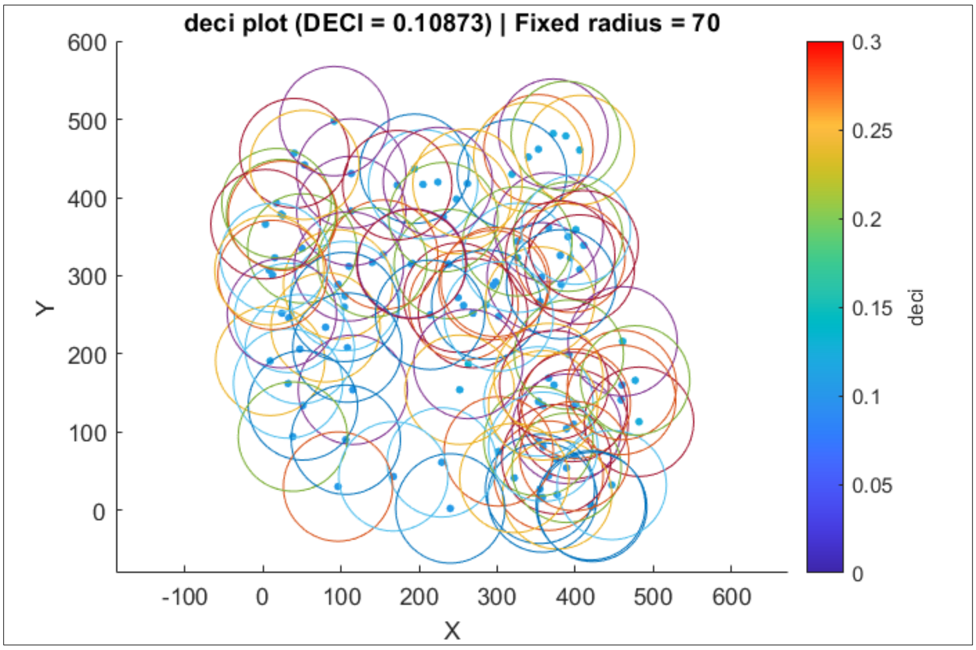

Figure 17. *DECI* and $deci$ values for *D1* with a search radius of 70.

As can be discerned from the previous figures, the increase in *DECI* is not guaranteed, and it will not follow a linear pattern, as it is contingent on the arrangement of data points. **Figure 18** depicts the *DECI* trend as the search radius varies and **Table 9** presents the previous findings in a tabular format, including the scenario where the radius is set to $+Inf$.

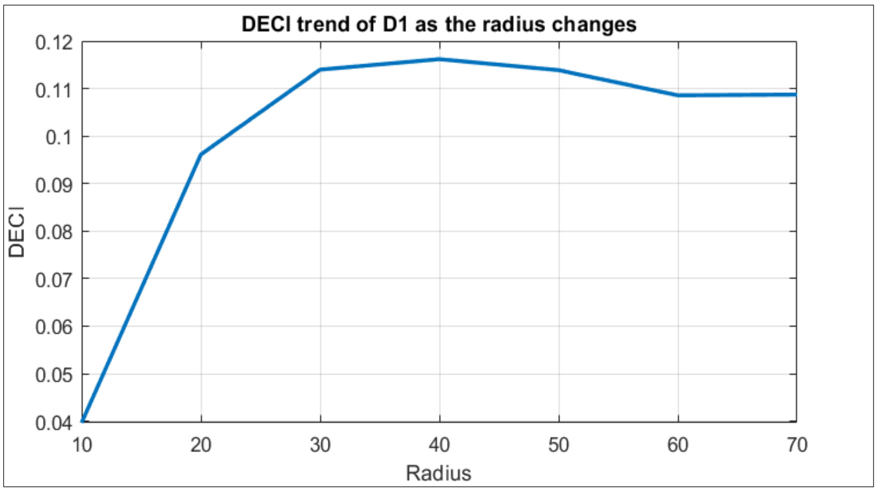

Figure 18. *DECI* trend of *D1* as the search radius varies.

Table 9. *DECI* values of *D1* as the search radius varies.

Radius	**DECI**
10	0.039662
20	0.096113
30	0.113980
40	0.116180
50	0.113870
60	0.108570
70	0.108730
+Inf	0.078814

As noted by the previously presented considerations, assuming that the values of *deci* (and, consequently, the values of *DECI*) are null with search radius equal to zero, an initial increase in the *DECI* value for the distribution is observed as the search radius expands. Nevertheless, in contrast to the linear increase in radius value, *DECI* increment becomes progressively less prominent, culminating when the search radius attains a value of 40. This can be attributed to the initial predominance of the effect of incorporating neighbouring points within the search radius of each data point. Subsequently, the prevailing influence pertains to the spatial arrangement of the data points. Indeed, *DECI* takes into account not only the proximity of data points but also their positioning within the plane (or in space).

Figure 19 now displays *D1*, with data points assigned variable search radii.

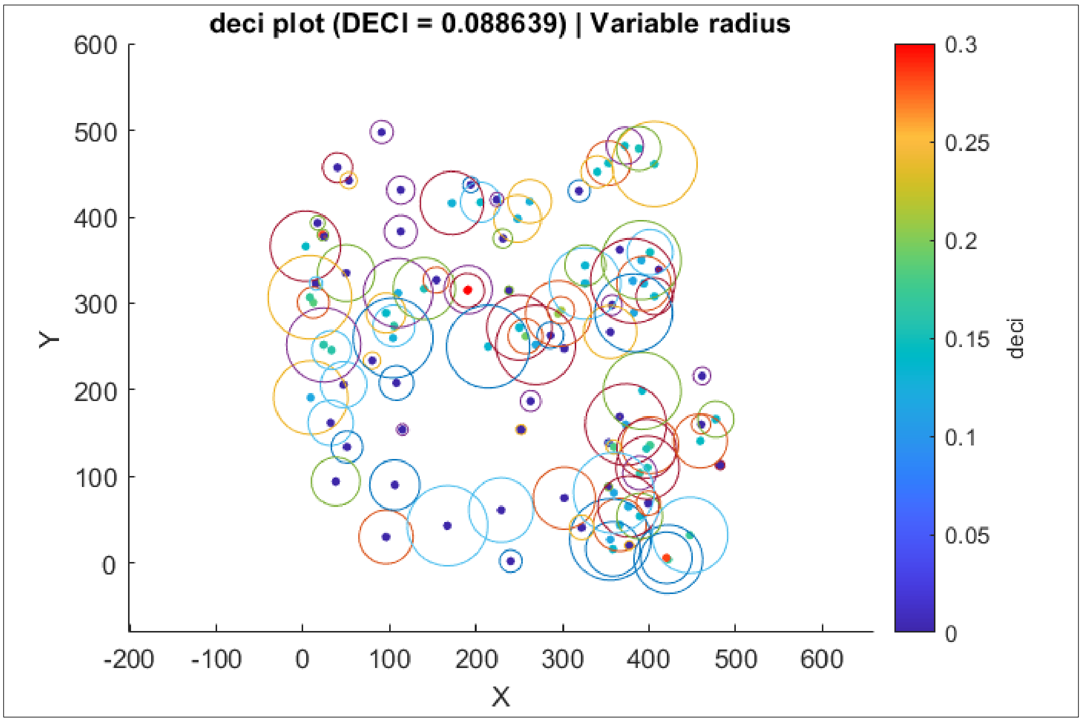

Figure 19. *DECI* and *deci* values for *D1* with a variable search radius.

The utilisation of a variable radius proves advantageous when considering the assignment of weights to individual data points. *DECI*, apart from being proposed as a method for describing a point cloud, holds the potential to be applied to a point cloud where these data points do not represent the geometry of a scanned object but rather serve as constituents of a system, encompassing objects of the same category dispersed in space, each possessing distinct characteristics. One conceivable application of *DECI* is in the capacity of serving as an indicator for congestion and risk within the transportation system. Notably, the data points could represent a range of vehicles, including cars, ships, and aircraft, each characterised by differing dimensions and speeds. Consequently, it is considered viable to tailor the radius, in proportion to both the velocity and size of the vehicle, alongside the potential hazards associated with the transported cargo. For instance, a significantly large and fast-moving vehicle offers heightened prospects for engagement with data points positioned at a greater distance, when compared to a smaller, slower, or stationary vehicle, thus exemplifying its adaptability and versatility in diverse transportation contexts.

3.4.3 Case study: DECI for maritime navigation risk assessment in the Strait of Messina

Context

The ongoing surge in vessel traffic is associated with an escalated likelihood of encountering highly congested waterways. This, in turn, augments the risk of maritime incidents such as collisions, which can have potentially catastrophic consequences, not only in terms of human lives but also economically and environmentally. To avert such unwelcome occurrences, various risk mitigation measures are presently implemented through the monitoring and management of maritime traffic. These measures encompass Traffic Separation Scheme (TSS), the establishment of areas governed by the Vessel Traffic Service (VTS), and pilotage, whether in a physical or remote capacity. These risk mitigation measures are selectively deployed, focusing on areas considered to be potentially more perilous. The utilisation of these measures necessitates a financial commitment by the state. In cases where resources are constrained, a judicious selection must be made regarding which risk mitigation measure to activate and, more crucially, in which areas to apply them. Consequently, it becomes imperative to compare multiple ports or navigable regions to ascertain how resources can be invested to enhance safety. However, the comparison of two or more dissimilar navigable areas is a non-trivial task. This complexity arises from the inherent differences in morphology, the intensity and type of maritime traffic, which consistently distinguish one area from another.

Several studies have been conducted over the years with the aim of assessing the risk associated with navigation in particular waterways considered interesting from the point of view of risk analysis. Some of them assess the risk based on the probability of collision or grounding phenomena occurring. Other studies instead focus on the analysis of maritime traffic looking for a risk index to be associated with the investigated area and, sometimes, dividing that area into several micro-areas with different risk index.

In accordance with the aforementioned considerations, it becomes evident that there is a pressing requirement for the development of a comprehensive risk index associated with the waterway under investigation. This index should not rely solely on the historical data of past accidents, which are typically few in number and hold limited statistical significance. Moreover, it should not be directly proportional to the number of ships in the area. This is because an equal quantity of vessels in a given area may assume different spatial configurations, consequently affecting the risk of accidents or traffic congestion.

The intent of this case study is to use the *DECI* of the distribution of ships considered as a point cloud to establish a quantitative measure, also observable in real time, which reflects the potential level of risk of the navigable area.

The used dataset for this application is composed by the “Automatic Identification System” (AIS) data. AIS data comprises information exchanged between ships and coastal stations to monitor and exchange navigation data. This system is widely employed to enhance safety, efficiency, and the management of maritime traffic. It finds utility among various stakeholders in the maritime sector, including ship operators, port authorities, maritime authorities, search and rescue services, maritime insurance companies, and other organizations involved in overseeing maritime traffic. AIS empowers ships to transmit, at predefined time intervals, and receive a wide array of information, including ship identification (name and unique identification number), location (latitude and longitude), navigation data (e.g., position time stamp, speed, and course), operating state (indicating whether ships are anchored, in motion, or operating under specific conditions), and ship static data (e.g., cargo type, length, width, height, and draught)[8]. In the context of this research, the AIS data used (granted by the Italian Coast Guard of Messina) cover a period of twelve months (from June 2018 to May 2019), specifically

---

[8] Resolution A.1106(29) by International Maritime Organization (IMO).

referring to the Strait of Messina (Italy). The entire available dataset consists of 22,794,085 instances.

For the specific application, the following AIS information is utilised: name, position time stamp, latitude, longitude, speed, and length. The name attribute serves the purpose of uniquely identifying a vessel. The position time stamp information is employed to establish the chosen time window for analysis. Latitude and longitude data are used to specify the position of the point cloud in the space, while speed and length are employed to determine the appropriate radius for the *DECI* evaluation. To enable a more precise analysis, it becomes necessary to correlate a ship's size and speed with the size of its neighbourhood. As a result, all the relevant quantities are expressed in degrees of latitude (or longitude).

In particular, speed is converted from knots (kn) to degrees per second (deg/s), and the ship's length is transformed from meters to degrees. It's important to note that degrees of latitude (or longitude) do not correspond to consistent distances in meters across different locations on the Earth's surface. To analyse small sections of the sea, the reasonable approximation of treating the Earth as a sphere were made. Under this assumption, one degree of latitude is considered equivalent to one degree of longitude, and both represent the same distance in meters. Specifically, the Earth is approximated as a sphere with a radius of 6,371,000 meters, which represents the average value [136]. Employing this value, all required lengths are converted into degrees denoted as α, using the following formula that takes into account the small-angle approximation:

$$\alpha = \frac{Length\ in\ meters}{Earth's\ radius\ in\ meters} \cdot \frac{180}{\pi} \tag{24}$$

This approach facilitates the analysis of small-scale marine environments, as it provides a practical way to equate geographic degrees to consistent measurements for various parameters.

The search radius to be used for the evaluation of differential entropy was chosen to be variable for each point (ship) according to the formula:

$$r = c_m \cdot \sqrt{\lambda} \tag{25}$$

Where λ represents the largest eigenvalue of the $\sum$ associated with the entire distribution p_n and c_m is a multiplicative coefficient defined as follow:

$$c_m = 1000 \cdot \sqrt{\frac{speed \cdot t \cdot lenght}{d_{min}}} \tag{26}$$

Where:

- $speed$ is evaluated in deg/s
- t is the average time intercurrent between two consecutive AIS signals transmitted by a ship
- $lenght$ is evaluated in deg
- d_{min} is the distance from the nearest ship (in deg).

In particular, the product of $speed$ and t represents the distance that the ship would navigate between two consecutive AIS signals. The coefficient 1000 was determined heuristically for the specific scenario. It is important to note that r depends on the entire distribution, the speed and length of the ship, as well as the minimum distance from the nearest ship. It's worth mentioning that r has dimensions of degrees, and it equals 0 if the ship has a null speed, indicating that it is stationary. This is in accordance with a risk index, where a stationary ship poses no collision risk due to its lack of movement, resulting in a *deci* value equal to zero. The other scenario in which a ship's *deci* is equal to zero is when there are no points within its neighbourhood.

In the context of the *DECI* evaluation pertaining to the Strait of Messina, AIS data was examined with a sampling frequency of 60 seconds. Consequently, for each minute under consideration, a series of 2D data points were generated to represent the positions of ships within the specified time interval in the sea area of interest. A search radius, in accordance with the Equation 25, was assigned to each data point. The *DECI* was subsequently calculated on a minute-by-minute basis for each of the 12 months available. From this analysis, the following data was derived:

- Maximum, minimum, and average *DECI* values for each month (**Table 10**)
- The average *DECI* value for each time interval (0-23) within each month (**Figure 20**).

Due to the substantial range in the order of magnitude of the detected *DECI* values, with an average of approximately 10^8 nat, a logarithmic representation was employed, utilizing the natural logarithm to express this data[9].

Table 10. Maximum, minimum, and mean *DECI* values for each month.

Month	**Max**	**Min**	**Mean**
January	25.51	5.22	19.08
February	29.89	0	23.39
March	29.49	5.94	22.96
April	23.93	0	18.22
May	25.04	0	19.32
June	26.81	0	20.29
July	24.88	5.31	18.69
August	29.25	4.99	22.65
September	22.71	0	17.31
October	23.24	5.45	17.74
November	31.47	3.70	24.90
December	30.55	6.01	23.96

Table 10 provides an overview of the maximum, minimum, and average *DECI* values for each month. The highest maximum value was recorded in June 2018, with a value of 31.48, while the lowest maximum value occurred in April,

---

[9] DECI values that are equal to zero are also treated as zero on the logarithmic scale.

at 22.71. The minimum *DECI* value observed is 0, signifying instances where ships are either stationary or where a ship's search radius is so constrained that it does not encompass other vessels within its range. In terms of average values, they range between a minimum of 11.43 and a maximum of 12.84.

Figure 20 illustrates the average *DECI* trend for each month, divided into time slots.

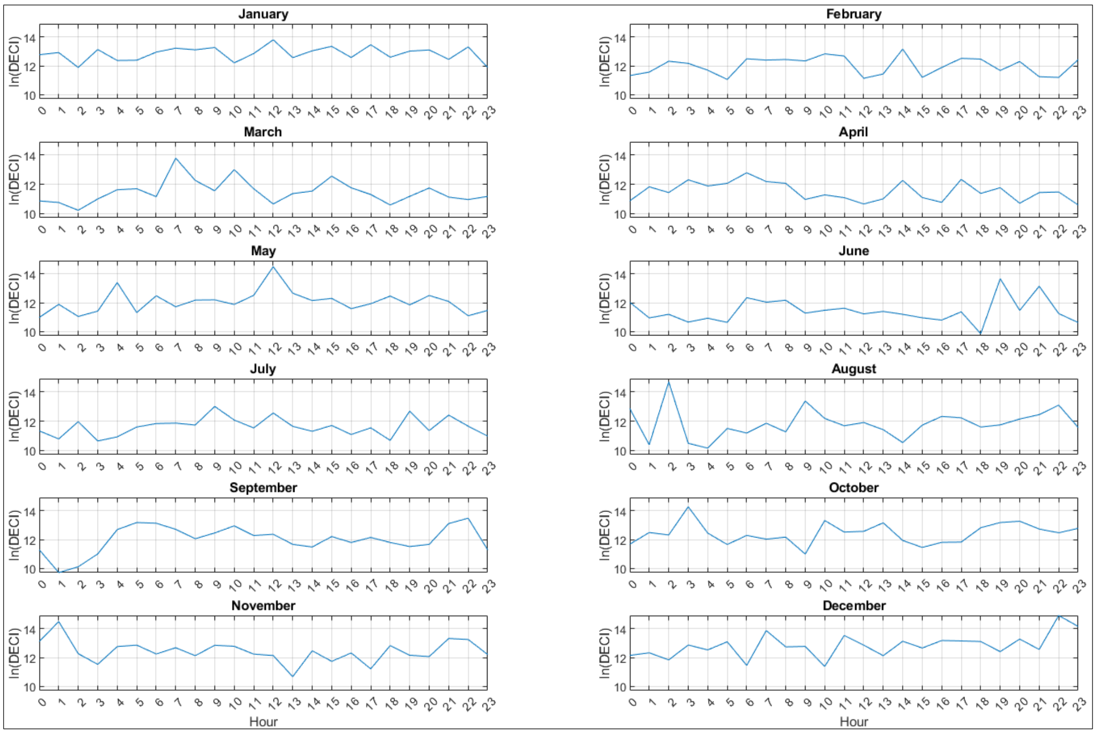

Figure 20. The average *DECI* value for each time interval (0-23) within each month.

These graphs enable the identification of the hours that are, on average, most congested, with variations from one month to another.

As an example, a snapshot (**Figure 21**) of the Strait of Messina is presented, associated with a *DECI* value of 17.36 and a total of 22 ships, of which 8 are in motion, as indicated by their non-zero search radius.

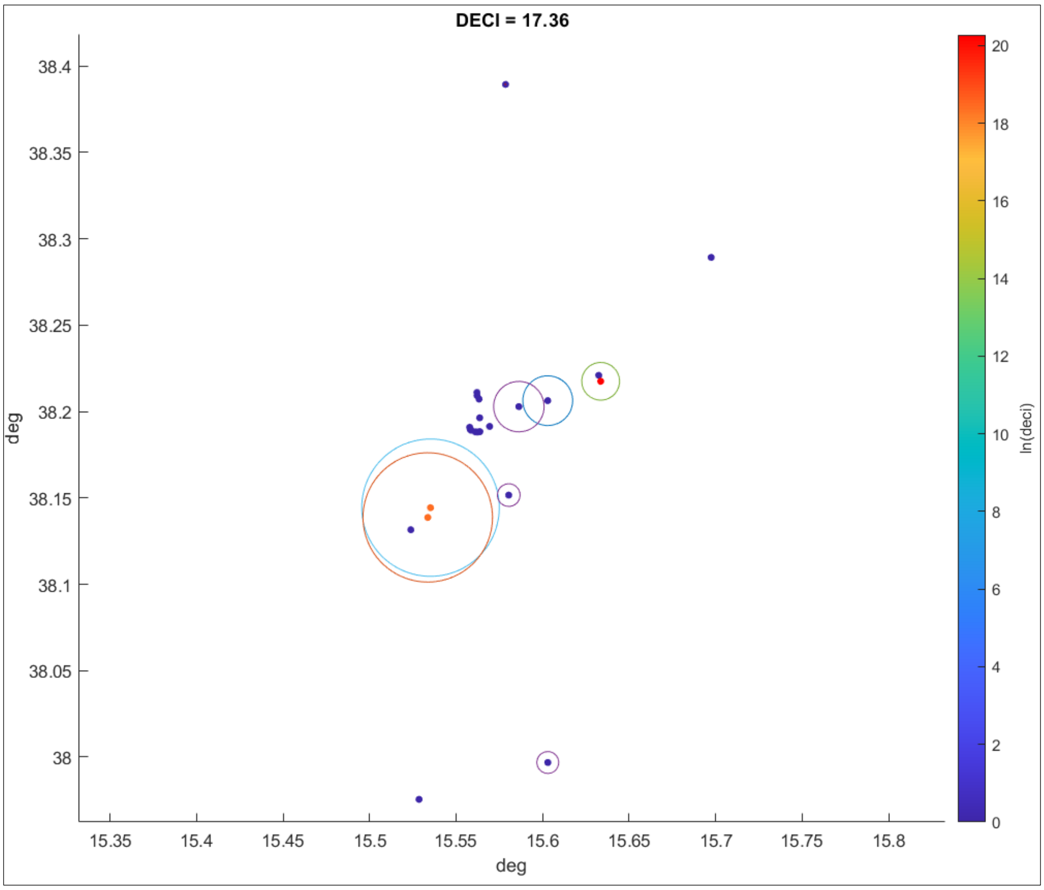

Figure 21. Example of application in the Strait of Messina.

In **Figure 21,** a point with the highest *deci* value is clearly visible, located in close proximity to a point with a *deci* of zero, which suggests the presence of a stationary ship. Additionally, there are four moving ships that can be observed, characterised by a *deci* of zero since there are no other ships within their respective search radius. On the other hand, the orange dots display an identical *deci* value because the same ships are encompassed within the search radius of each of them.

In **Figure 22**, the hourly trend of *DECI* on a specific day is depicted, with snapshots representing the first minute of each hour. This day was chosen as an example. Furthermore, data is supplied regarding the number of ships present in each of these snapshots.

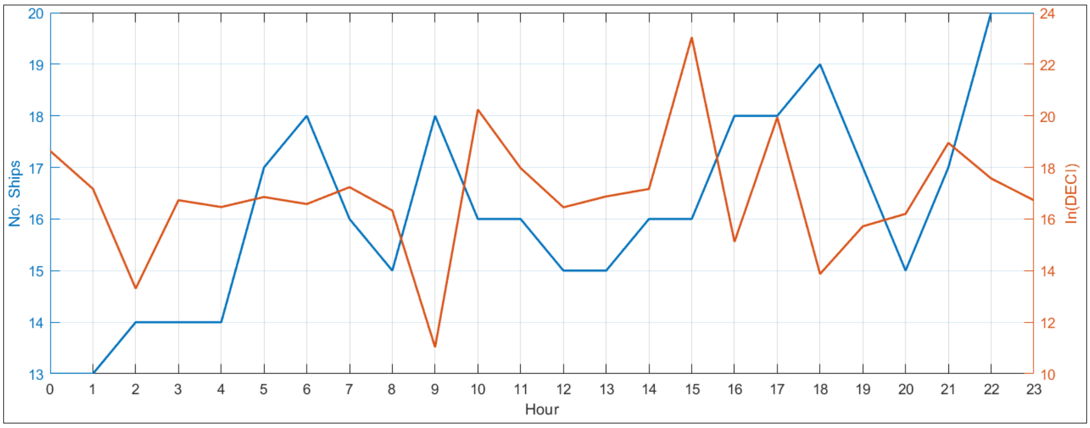

Figure 22. Hourly trend of *DECI* and number of ships on a specific day.

The comparison with the number of ships was conducted to emphasise that *DECI* does not exhibit a direct correlation with the number of ships. As illustrated, for instance, at 9:00, there is a relative minimum in *DECI* and a relative maximum in the number of ships, while at 23:00, the opposite situation occurs. This suggests that *DECI* is not directly affected by the number of ships.

4 CONCLUSIONS

The research carried out in this thesis focused on the study and application of point cloud analysis using differential entropy. This study has led to the development of novel formulations, innovative research methods, and the identification of alternatives to existing methods, overcoming many previous limitations.

A comprehensive analysis of the mathematical concepts underpinning differential entropy, as a measure of information within the data (point clouds), as well as statistical concepts and linear algebra associated with the inclusion of the covariance matrix and its determinant in the formulation, has resulted in a new formulation of differential entropy for both univariate and multivariate normal distributions. This modification ensures that the logarithmic argument in the formula is always greater than or equal to 1. This modification brings two significant advantages, particularly in conjunction with other innovations presented in this work. It resolves the issue of nullifying the determinant of the covariance matrix and guarantees that the differential entropy value for each point is always greater than or equal to zero. This newly developed formulation, tailored specifically for the analysis of 2D and 3D point clouds, has given rise to two distinct innovations in separate domains. The introduction of the *DEDA* method for conducting geometric deviation analyses, primarily designed for industrial applications such as quality control, has proven to be highly effective. Unlike traditional methods based on Euclidean distance, which rely on mean and standard deviation for global assessment, the method proposed in this thesis, based on the new differential entropy formulation, not only enjoys commutative properties in evaluating differences but also provides a synthetic quality index. This index quantitatively assesses the conformity of a manufactured piece to its virtual model. Additionally, like traditional deviation analysis, it allows the visualization of a point cloud with color-coded points to identify areas that deviate the most from the model's geometry. This capability aids in identifying manufacturing issues and enables preventive measures, such as modifying the CAD model in areas with significant shrinkage in the case of AM using FDM technology. The *DEDA* method has also shown resilience in evaluating challenging cases involving noise, background interference, holes in the point cloud, partial overlap, and density variations between the compared point clouds.

The introduction of the *DECI*, based on the new differential entropy formulation for univariate and multivariate distributions, has enabled the development of a novel point cloud analysis method. *DECI* provides a synthetic quantitative index describing the point cloud under consideration, particularly suitable for systems represented as point clouds. Its immediate application lies in the field of transportation, as demonstrated in the case study of maritime traffic analysis in the Strait of Messina (Italy), where *DECI* serves as a risk and congestion index for the affected sea area. The ability to use AIS data, which includes real-time ship information, has allowed for both real-time and retrospective analyses. By applying *DECI* to the point cloud created from AIS data, it was possible to assess risk and congestion on an hourly, monthly, and annual basis. This analysis revealed minimum, average, and maximum values and the index's trend, providing insights into congested time intervals and forming the basis for congestion mitigation measures in affected sea areas. The *DECI* index's unique feature is its independence from the number of points but instead depends on their spatial distribution and interactions, as determined by the search radius.

In terms of future developments stemming from the innovations in this thesis, there are several potential avenues to explore.

With regards to the *DEDA* method, it could be extended to compare multiple objects to determine which one best matches the model in terms of geometric fidelity. Furthermore, the robustness of *DEDA* in the presence of noise, holes, and density variations suggests the potential for a novel point cloud registration method that can address these limitations more effectively than the conventional ICP method. Such a method, based on the new formulation of differential entropy, could iteratively minimise the quality index, offering a robust alternative to ICP.

DECI, while initially applied in the maritime sector, demonstrates significant potential for diverse applications in the broader field of transportation, including road traffic, aviation, and drones. These applications could help identify congested areas, facilitating not only transportation planning but also environmental analysis for urban planning purposes. The versatility of *DECI* extends to various domains, making it a valuable tool in different contexts. It can be applied to crowd analysis, especially in safety and healthcare settings, such as managing overcrowded situations like the COVID-19 epidemic. Additionally, *DECI* has potential commercial applications, as it could be employed in museums to draw attention to specific objects by placing them in areas with high *DECI* values. *DECI*'s utility can also be seen in the analysis of team sports, such as football. It could be used to evaluate a team's *DECI* trend, considering players as points, both in temporal and spatial terms. This analysis could reveal correlations between *DECI* and key actions or match outcomes. Similarly, *DECI* could find use in monitoring groups of animals, enabling the analysis of their movements and identification of behavioural patterns. In medicine, *DECI* could be valuable for analysing the distribution and evolution of specific cells, like tumour cells or reproductive cells, to identify correlations with disease stage and fertility. In materials science, particularly in metallic materials, *DECI* could be employed to analyse the distribution of defects or unwanted inclusions within the material, seeking correlations with its mechanical properties. Finally, in the context of topology optimization, especially in AM production, *DECI* could be used to create variable density structural components, offering new possibilities for enhancing materials and manufacturing processes.

REFERENCES

1. Carmigniani, J.; Furht, B. Augmented Reality: An Overview BT - Handbook of Augmented Reality. In; Furht, B., Ed.; Springer New York: New York, NY, 2011; pp. 3–46 ISBN 978-1-4614-0064-6.
2. Wohlgenannt, I.; Simons, A.; Stieglitz, S. Virtual Reality. *Bus. Inf. Syst. Eng.* **2020**, *62*, 455–461, doi:10.1007/s12599-020-00658-9.
3. Vagvolgyi, B.; Niu, W.; Chen, Z.; Wilkening, P.; Kazanzides, P. Augmented Virtuality for Model-Based Teleoperation. *IEEE Int. Conf. Intell. Robot. Syst.* **2017**, *2017-Septe*, 3826–3833, doi:10.1109/IROS.2017.8206233.
4. Chang, G.; Morreale, P.; Medicherla, P. Applications of Augmented Reality Systems in Education. In Proceedings of the Proceedings of SITE 2010--Society for Information Technology & Teacher Education International Conference; D. Gibson & B. Dodge, 2010; pp. 1380–1385.
5. Sorko, S.R.; Brunnhofer, M. Potentials of Augmented Reality in Training. *Procedia Manuf.* **2019**, *31*, 85–90, doi:10.1016/j.promfg.2019.03.014.
6. Plamadeala, V.; Dintu, S. Driver or Autopilot – Who Is the Future. *J. Eng. Sci.* **2022**, *29*, 48–61, doi:10.52326/jes.utm.2022.29(1).04.
7. Ingle, S.; Phute, M. Tesla Autopilot : Semi Autonomous Driving, an Uptick for Future Autonomy. *Int. Res. J. Eng. Technol.* **2016**, *3*, 369–372.

8. Dikmen, M.; Burns, C.M. Autonomous Driving in the Real World: Experiences with Tesla Autopilot and Summon. *Proc. 8th Int. Conf. Automot. User Interfaces Interact. Veh. Appl. Assoc. Comput. Mach. (Automotive'UI 16)* **2016**, 225–228, doi:https://doi.org/10.1145/3003715.3005465.
9. Chen, S.; Liu, B.; Feng, C.; Vallespi-Gonzalez, C.; Wellington, C. 3D Point Cloud Processing and Learning for Autonomous Driving: Impacting Map Creation, Localization, and Perception. *IEEE Signal Process. Mag.* **2021**, *38*, 68–86, doi:10.1109/MSP.2020.2984780.
10. Chen, Q.; Ma, X.; Tang, S.; Guo, J.; Yang, Q.; Fu, S. F-Cooper: Feature Based Cooperative Perception for Autonomous Vehicle Edge Computing System Using 3D Point Clouds. *Proc. 4th ACM/IEEE Symp. Edge Comput. SEC 2019* **2019**, 88–100, doi:10.1145/3318216.3363300.
11. Singandhupe, A.; La, H. A Review of SLAM Techniques and Security in Autonomous Driving. *Proc. - 3rd IEEE Int. Conf. Robot. Comput. IRC 2019* **2019**, 602–607, doi:10.1109/IRC.2019.00122.
12. Javaid, M.; Haleem, A.; Singh, R.P.; Suman, R. 3D Printing Applications for Healthcare Research and Development. *Glob. Heal. J.* **2022**, *6*, 217–226, doi:10.1016/j.glohj.2022.11.001.
13. Aimar, A.; Palermo, A.; Innocenti, B. The Role of 3D Printing in Medical Applications: A State of the Art 2019, Article ID 5340616. *J. Healthc. Eng.* **2019**, *2019*, 10.
14. Kariyawasam, R.S.; Song, M.-K. (Kevin); Kodali, P.; Chen, A.; Domi, A.; Cai, J.; Almoamen, E.; Rajapakse, C.S. Automated Medical Image Based Anatomical Point Cloud Generation for Collaborative Real-Time Augmented Reality Applications. In Proceedings of the Proc.SPIE; April 4 2022; Vol. 12037, p. 120370R.
15. Yoo, S.J.; Spray, T.; Austin, E.H.; Yun, T.J.; van Arsdell, G.S. Hands-on Surgical Training of Congenital Heart Surgery Using 3-Dimensional Print Models. *J. Thorac. Cardiovasc. Surg.* **2017**, *153*, 1530–1540, doi:10.1016/j.jtcvs.2016.12.054.
16. Hoashi, T.; Ichikawa, H.; Nakata, T.; Shimada, M.; Ozawa, H.; Higashida, A.; Kurosaki, K.; Kanzaki, S.; Shiraishi, I. Utility of a Super-Flexible Three-Dimensional Printed Heart Model in Congenital Heart Surgery. *Interact. Cardiovasc. Thorac. Surg.* **2018**, *27*, 749–755, doi:10.1093/icvts/ivy160.
17. Spinelli, D.; La Corte, F.; Cucinotta, F.; Barberi, E.; Benedetto, F. A Deep Learning Model for the Prediction of Complications After EVAR Based on Pre-Operative Aneurysm Morphology. *EJVES Vasc. Forum* **2022**, *54*, e60.
18. Somma, R.; Altadonna, A.; Cucinotta, F.; Raffaele, M.; Salmeri, F.; Baldino, G.; Spagnolo, E.V.; Sapienza, D. The Technologies of Laser Scanning and Structured Blue Light Scanning Applied to Criminal Investigation: Case Studies. *Atti della Accad. Peloritana dei Pericolanti - Cl. di Sci. Fis. Mat. e Nat. Vol 101, SUPPL NO 1 Adv. Appl. Geoforensics Unraveling Crimes with Geol.* **2023**, doi:10.1478/AAPP.101S1A15.
19. Wang, J.; Li, Z.; Hu, W.; Shao, Y.; Wang, L.; Wu, R.; Ma, K.; Zou, D.; Chen, Y. Virtual Reality and Integrated Crime Scene Scanning for Immersive and Heterogeneous Crime Scene Reconstruction. *Forensic Sci. Int.* **2019**, *303*, 109943, doi:10.1016/j.forsciint.2019.109943.
20. Amamra, A.; Amara, Y.; Boumaza, K.; Benayad, A. Crime Scene

Reconstruction with RGB-D Sensors. *Proc. 2019 Fed. Conf. Comput. Sci. Inf. Syst. FedCSIS 2019* **2019**, *18*, 391–396, doi:10.15439/2019F225.

21. Liu, S. Three-Dimension Point Cloud Technology and Intelligent Extraction of Trace Evidence at the Scene of Crime. *J. Phys. Conf. Ser.* **2019**, *1237*, doi:10.1088/1742-6596/1237/4/042027.
22. Bostanci, E. 3D Reconstruction of Crime Scenes and Design Considerations for an Interactive Investigation Tool. **2015**, *4*, 50–58.
23. Guarnera, L.; Giudice, O.; Livatino, S.; Paratore, A.B.; Salici, A.; Battiato, S. Assessing Forensic Ballistics Three-Dimensionally through Graphical Reconstruction and Immersive VR Observation. *Multimed. Tools Appl.* **2022**, doi:10.1007/s11042-022-14037-x.
24. Zhang, H.; Gu, J.; Chen, J.; Sun, F.; Wang, H. Pilot Study of Feature-Based Algorithm for Breech Face Comparison. *Forensic Sci. Int.* **2018**, *286*, 148–154, doi:10.1016/j.forsciint.2018.02.026.
25. Kara, I.; Karatatar, A. Classification of Fired Cartridge Cases Using 3D Image Capture and a Comparison of Database Correlation Method Performance. *J. Forensic Sci.* **2022**, *67*, 1998–2008, doi:10.1111/1556-4029.15089.
26. Sivanandan1, J.; Liscio1, E.; Eng, P. Article Assessing Structured Light 3D Scanning Using Artec Eva for Injury Documentation during Autopsy Article. *J Assoc Crime Scene Reconstr* **2017**, 21.
27. Levoy, M.; Pulli, K.; Curless, B.; Rusinkiewicz, S.; Koller, D.; Pereira, L.; Ginzton, M.; Anderson, S.; Davis, J.; Ginsberg, J.; et al. The Digital Michelangelo Project: 3D Scanning of Large Statues. *SIGGRAPH 2000 - Proc. 27th Annu. Conf. Comput. Graph. Interact. Tech.* **2000**, 131–144, doi:10.1145/344779.344849.
28. Pieraccini, M.; Guidi, G.; Atzeni, C. 3D Digitizing of Cultural Heritage. *J. Cult. Herit.* **2001**, *2*, 63–70, doi:10.1016/S1296-2074(01)01108-6.
29. Canevese, E.P.; De Gottardo, T. Beyond Point Clouds and Virtual Reality Innovative Methods and Technologies for the Protection and Promotion of Cultural Heritage. *Int. Arch. Photogramm. Remote Sens. Spat. Inf. Sci. - ISPRS Arch.* **2017**, *42*, 685–691, doi:10.5194/isprs-Archives-XLII-5-W1-685-2017.
30. Mancini, F.; Dubbini, M.; Gattelli, M.; Stecchi, F.; Fabbri, S.; Gabbianelli, G. Using Unmanned Aerial Vehicles (UAV) for High-Resolution Reconstruction of Topography: The Structure from Motion Approach on Coastal Environments. *Remote Sens.* **2013**, *5*, 6880–6898, doi:10.3390/rs5126880.
31. Moon, D.; Chung, S.; Kwon, S.; Seo, J.; Shin, J. Comparison and Utilization of Point Cloud Generated from Photogrammetry and Laser Scanning: 3D World Model for Smart Heavy Equipment Planning. *Autom. Constr.* **2019**, *98*, 322–331, doi:10.1016/j.autcon.2018.07.020.
32. Kregar, K.; Vrabec, M.; Grigillo, D. Developing a Robust Workflow for Acquisition of High-Resolution Full-3D Cave Topography, Surface Topography Integration, and Digital Structural Mapping. *Geophys. Res. Abstr.* **2019**, *21*.
33. Cucchiaro, S.; Cavalli, M.; Vericat, D.; Crema, S.; Llena, M.; Beinat, A.; Marchi, L.; Cazorzi, F. Monitoring Topographic Changes through 4D-Structure-from-Motion Photogrammetry: Application to a Debris-Flow Channel. *Environ. Earth Sci.* **2018**, *77*, 1–21, doi:10.1007/s12665-018-7817-4.
34. Grenzdörffer, G.J. Crop Height Determination with UAS Point Clouds. *Int.*

Arch. Photogramm. Remote Sens. Spat. Inf. Sci. - ISPRS Arch. **2014**, *40*, 135–140, doi:10.5194/isprsarchives-XL-1-135-2014.

35. Minhui, L.; Shamshiri, R.R.; Schirrmann, M.; Weltzien, C. Impact of Camera Viewing Angle for Estimating Leaf Parameters of Wheat Plants from 3d Point Clouds. *Agric.* **2021**, *11*, doi:10.3390/agriculture11060563.
36. Itakura, K.; Hosoi, F. Automatic Leaf Segmentation for Estimating Leaf Area and Leaf Inclination Angle in 3D Plant Images. *Sensors (Switzerland)* **2018**, *18*, doi:10.3390/s18103576.
37. De Souza, C.H.W.; Lamparelli, R.A.C.; Rocha, J.V.; Magalhães, P.S.G. Height Estimation of Sugarcane Using an Unmanned Aerial System (UAS) Based on Structure from Motion (SfM) Point Clouds. *Int. J. Remote Sens.* **2017**, *38*, 2218–2230, doi:10.1080/01431161.2017.1285082.
38. Wang, X.; Pan, H.; Guo, K.; Yang, X.; Luo, S. The Evolution of LiDAR and Its Application in High Precision Measurement. *IOP Conf. Ser. Earth Environ. Sci.* **2020**, *502*, doi:10.1088/1755-1315/502/1/012008.
39. Nelson, R. How Did We Get Here? An Early History of Forestry Lidar1. *Can. J. Remote Sens.* **2013**, *39*, S6–S17, doi:10.5589/m13-011.
40. Raj, T.; Hashim, F.H.; Huddin, A.B.; Ibrahim, M.F.; Hussain, A. A Survey on LiDAR Scanning Mechanisms. *Electron.* **2020**, *9*, doi:10.3390/electronics9050741.
41. Li, Y.; Ibanez-Guzman, J. *IEEE Signal Processing Magazine*. 2020, pp. 50–61.
42. Behroozpour, B.; Sandborn, P.A.M.; Wu, M.C.; Boser, B.E. Lidar System Architectures and Circuits. *IEEE Commun. Mag.* **2017**, *55*, 135–142, doi:10.1109/MCOM.2017.1700030.
43. Rubinsztein-Dunlop; Halina; Forbes, A.; Berry, M. V.; Dennis, M.R.; Andrews, D.L.; Mansuripur, M.; Denz, C. Roadmap on Structured Light. *J. Opt. (United Kingdom)* **2016**, *19*, 013001.
44. Bell, T.; Li, B.; Zhang, S. Structured Light Techniques and Applications. *Wiley Encycl. Electr. Electron. Eng.* **2016**, 1–24, doi:10.1002/047134608x.w8298.
45. Long, F.; Zhou, J.; Peng, H. Visualization and Analysis of 3D Microscopic Images. *PLoS Comput. Biol.* **2012**, *8*, doi:10.1371/journal.pcbi.1002519.
46. Myshkin, N.K.; Grigoriev, A.Y.; Chizhik, S.A.; Choi, K.Y.; Petrokovets, M.I. Surface Roughness and Texture Analysis in Microscale. *Wear* **2003**, *254*, 1001–1009, doi:10.1016/S0043-1648(03)00306-5.
47. Elliott, A.D. Confocal Microscopy: Principles and Modern Practices. *Curr. Protoc. Cytom.* **2020**, *92*, e68, doi:https://doi.org/10.1002/cpcy.68.
48. Artigas, R. Imaging Confocal Microscopy BT - Optical Measurement of Surface Topography. In; Leach, R., Ed.; Springer Berlin Heidelberg: Berlin, Heidelberg, 2011; pp. 237–286 ISBN 978-3-642-12012-1.
49. Bayguinov, P.O.; Oakley, D.M.; Shih, C.-C.; Geanon, D.J.; Joens, M.S.; Fitzpatrick, J.A.J. Modern Laser Scanning Confocal Microscopy. *Curr. Protoc. Cytom.* **2018**, *85*, e39, doi:https://doi.org/10.1002/cpcy.39.
50. Artigas, R.; Matilla, A.; Mariné, J.; Pérez, J.; Cadevall, C. Three-Dimensional Measurements with a Novel Technique Combination of Confocal and Focus Variation with a Simultaneous Scan. *Proc. 16th Int. Conf. Eur. Soc. Precis. Eng. Nanotechnology, EUSPEN 2016* **2016**, *9890*, 1–11, doi:10.1117/12.2227054.
51. Schwarz, C.J.; Kuznetsova, Y.; Brueck, S.R.J. Imaging Interferometric Microscopy. *OSA Trends Opt. Photonics Ser.* **2003**, *88*, 1354–1356.

52. Luhmann, T. Close Range Photogrammetry for Industrial Applications. *ISPRS J. Photogramm. Remote Sens.* **2010**, *65*, 558–569, doi:10.1016/j.isprsjprs.2010.06.003.
53. Buzug, T.M. Computed Tomography BT - Springer Handbook of Medical Technology. In; Kramme, R., Hoffmann, K.-P., Pozos, R.S., Eds.; Springer Berlin Heidelberg: Berlin, Heidelberg, 2011; pp. 311–342 ISBN 978-3-540-74658-4.
54. Garba, I.; Zarb, F.; McEntee, M.F.; Fabri, S.G. Computed Tomography Diagnostic Reference Levels for Adult Brain, Chest and Abdominal Examinations: A Systematic Review. *Radiography* **2021**, *27*, 673–681, doi:10.1016/j.radi.2020.08.011.
55. Sun, W, Brown, S B, Leach, R.K. An Overview of Industrial X-Ray Computed Tomography. *NPL Report. ENG 32* 2012.
56. Hu, Z. ICP Algorithm for 3D Surface Registration. *Highlights Sci. Eng. Technol.* **2022**, *24*, 94–98, doi:10.54097/hset.v24i.3898.
57. Geng, Z.; Garcia, M.E.; Bidanda, B. Minimax Registration for Point Cloud Alignment. *Manuf. Lett.* **2022**, *33*, 872–879, doi:10.1016/j.mfglet.2022.07.108.
58. Zhang, S.; Yang, Y.; Yang, K.; Luo, Y.; Ong, S.H. Point Set Registration with Global-Local Correspondence and Transformation Estimation. *Proc. IEEE Int. Conf. Comput. Vis.* **2017**, *2017-Octob*, 2688–2696, doi:10.1109/ICCV.2017.291.
59. Lawin, F.J.; Forssen, P.E. Registration Loss Learning for Deep Probabilistic Point Set Registration. *Proc. - 2020 Int. Conf. 3D Vision, 3DV 2020* **2020**, 563–572, doi:10.1109/3DV50981.2020.00066.
60. Kurobe, A.; Sekikawa, Y.; Ishikawa, K.; Saito, H. CorsNet: 3D Point Cloud Registration by Deep Neural Network. *IEEE Robot. Autom. Lett.* **2020**, *5*, 3960–3966, doi:10.1109/LRA.2020.2970946.
61. Zhang, Z.; Dai, Y.; Sun, J. Deep Learning Based Point Cloud Registration: An Overview. *Virtual Real. Intell. Hardw.* **2020**, *2*, 222–246, doi:10.1016/j.vrih.2020.05.002.
62. Elbaz, G.; Avraham, T.; Fischer, A. 3D Point Cloud Registration for Localization Using a Deep Neural Network Auto-Encoder. In Proceedings of the 2017 IEEE Conference on Computer Vision and Pattern Recognition (CVPR); 2017; pp. 2472–2481.
63. Men, H.; Gebre, B.; Pochiraju, K. Color Point Cloud Registration with 4D ICP Algorithm. *Proc. - IEEE Int. Conf. Robot. Autom.* **2011**, 1511–1516, doi:10.1109/ICRA.2011.5980407.
64. Pomerleau, F.; Colas, F.; Siegwart, R.; Magnenat, S. Comparing ICP Variants on Real-World Data Sets: Open-Source Library and Experimental Protocol. *Auton. Robots* **2013**, *34*, 133–148, doi:10.1007/s10514-013-9327-2.
65. Rajendra, Y.D.; Mehrotra, S.C.; Kale, K. V.; Manza, R.R.; Dhumal, R.K.; Nagne, A.D.; Vibhute, A.D. Evaluation of Partially Overlapping 3D Point Cloud's Registration by Using ICP Variant and Cloudcompare. *Int. Arch. Photogramm. Remote Sens. Spat. Inf. Sci. - ISPRS Arch.* **2014**, *XL–8*, 891–897, doi:10.5194/isprsarchives-XL-8-891-2014.
66. Zhang, L.; Choi, S.I.; Park, S.Y. Robust ICP Registration Using Biunique Correspondence. *Proc. - 2011 Int. Conf. 3D Imaging, Model. Process. Vis. Transm. 3DIMPVT 2011* **2011**, 80–85, doi:10.1109/3DIMPVT.2011.18.

67. Douadi, L.; Aldon, M.J.; Crosnier, A. Pair-Wise Registration of 3D/Color Data Sets with ICP. *IEEE Int. Conf. Intell. Robot. Syst.* **2006**, 663–668, doi:10.1109/IROS.2006.282551.
68. Granger, S.; Pennec, X.; Roche, A. Rigid Point-Surface Registration Using an EM Variant of ICP for Computer Guided Oral Implantology BT - Medical Image Computing and Computer-Assisted Intervention – MICCAI 2001.; Niessen, W.J., Viergever, M.A., Eds.; Springer Berlin Heidelberg: Berlin, Heidelberg, 2001; pp. 752–761.
69. J. Besl, P.; D. McKay, N. A Method for Registration of 3-D Shapes. *IEEE Trans. Pattern Anal. Mach. Intell.* **1992**, *14*, 239–256.
70. Yang, C.; Medioni, G. Object Modelling by Registration of Multiple Range Images. *Image Vis. Comput.* **1992**, *10*, 145–155, doi:10.1016/0262-8856(92)90066-C.
71. Shen, Z.; Huang, G.; Zhi, P.; Zhao, R. Localization for Unmanned Vehicle. In *Theories and Practices of Self-Driving Vehicles*; Zhou, Q., Shen, Z., Yong, B., Zhao, R., Zhi, P., Eds.; Elsevier, 2022; pp. 63–93 ISBN 9780323994484.
72. Oomori, S.; Nishida, T.; Kurogi, S. Point Cloud Matching Using Singular Value Decomposition. *Artif. Life Robot.* **2016**, *21*, 149–154, doi:10.1007/s10015-016-0265-x.
73. Rusinkiewicz, S.; Levoy, M. Efficient Variants of the ICP Algorithm. *Proc. Int. Conf. 3-D Digit. Imaging Model. 3DIM* **2001**, 145–152, doi:10.1109/IM.2001.924423.
74. Laga, H. *A Survey on Nonrigid 3D Shape Analysis*; Elsevier Ltd., 2018; Vol. 6; ISBN 9780128119006.
75. Wujanz, D.; Schaller, S.; Gielsdorf, F.; Gründig, L. Plane-Based Registration of Several Thousand Laser Scans on Standard Hardware. *Int. Arch. Photogramm. Remote Sens. Spat. Inf. Sci. - ISPRS Arch.* **2018**, *42*, 1207–1212, doi:10.5194/isprs-archives-XLII-2-1207-2018.
76. Poreba, M.; Goulette, F. A Robust Linear Feature-Based Procedure for Automated Registration of Point Clouds. *Sensors (Switzerland)* **2015**, *15*, 1435–1457, doi:10.3390/s150101435.
77. Wang, Y.T.; Peng, C.C.; Ravankar, A.A.; Ravankar, A. A Single LiDAR-Based Feature Fusion Indoor Localization Algorithm. *Sensors (Switzerland)* **2018**, *18*, doi:10.3390/s18041294.
78. Salhi, I.; Poreba, M.; Piriou, E.; Gouet-BrunetValerie; Ojail, M. *Multimodal Localization for Embedded Systems: A Survey*; Elsevier Inc., 2019; ISBN 9780128173589.
79. Zhang, J.; Yao, Y.; Deng, B. Fast and Robust Iterative Closest Point. *IEEE Trans. Pattern Anal. Mach. Intell.* **2022**, *44*, 3450–3466, doi:10.1109/TPAMI.2021.3054619.
80. Lamine Tazir, M.; Gokhool, T.; Checchin, P.; Malaterre, L.; Trassoudaine, L. CICP: Cluster Iterative Closest Point for Sparse–Dense Point Cloud Registration. *Rob. Auton. Syst.* **2018**, *108*, 66–86, doi:10.1016/j.robot.2018.07.003.
81. Yue, X.; Liu, Z.; Zhu, J.; Gao, X.; Yang, B.; Tian, Y. Coarse-Fine Point Cloud Registration Based on Local Point-Pair Features and the Iterative Closest Point Algorithm. *Appl. Intell.* **2022**, 12569–12583, doi:10.1007/s10489-022-03201-3.

82. Yang, J.; Cao, Z.; Zhang, Q. A Fast and Robust Local Descriptor for 3D Point Cloud Registration. *Inf. Sci. (Ny).* **2016**, *346–347*, 163–179, doi:10.1016/j.ins.2016.01.095.
83. Ngo, T.D.; Kashani, A.; Imbalzano, G.; Nguyen, K.T.Q.; Hui, D. Additive Manufacturing (3D Printing): A Review of Materials, Methods, Applications and Challenges. *Compos. Part B Eng.* **2018**, *143*, 172–196, doi:10.1016/j.compositesb.2018.02.012.
84. Colosimo, B.M.; Huang, Q.; Dasgupta, T.; Tsung, F. Opportunities and Challenges of Quality Engineering for Additive Manufacturing. *J. Qual. Technol.* **2018**, *50*, 233–252, doi:10.1080/00224065.2018.1487726.
85. Rajan, K.; Samykano, M.; Kadirgama, K.; Harun, W.S.W.; Rahman, M.M. *Fused Deposition Modeling: Process, Materials, Parameters, Properties, and Applications*; Springer London, 2022; Vol. 120; ISBN 0017002208860.
86. Kumar, M.B.; Sathiya, P.; Varatharajulu, M. Selective Laser Sintering. In *Advances in Additive Manufacturing Processes*; China Bentham Books: Beijing, China, 2021; pp. 28–47.
87. Sefene, E.M. State-of-the-Art of Selective Laser Melting Process: A Comprehensive Review. *J. Manuf. Syst.* **2022**, *63*, 250–274, doi:10.1016/j.jmsy.2022.04.002.
88. Huang, J.; Qin, Q.; Wang, J. A Review of Stereolithography: Processes and Systems. *Processes* **2020**, *8*, doi:10.3390/PR8091138.
89. Muthuram, N.; Sriram Madhav, P.; Keerthi Vasan, D.; Mohan, M.E.; Prajeeth, G. A Review of Recent Literatures in Poly Jet Printing Process. *Mater. Today Proc.* **2022**, *68*, 1906–1920, doi:10.1016/j.matpr.2022.08.090.
90. Gibson, I.; Rosen, D.; Stucker, B.; Khorasani, M. Binder Jetting BT - Additive Manufacturing Technologies. In; Gibson, I., Rosen, D., Stucker, B., Khorasani, M., Eds.; Springer International Publishing: Cham, 2021; pp. 237–252 ISBN 978-3-030-56127-7.
91. Galati, M. Electron Beam Melting Process: A General Overview. In *Handbooks in Advanced Manufacturing*; Pou, J., Riveiro, A., Davim, J.P.B.T.-A.M., Eds.; Elsevier, 2021; pp. 277–301 ISBN 978-0-12-818411-0.
92. Mekonnen, B.G.; Bright, G.; Walker, A. A Study on State of the Art Technology of Laminated Object Manufacturing (LOM) BT - CAD/CAM, Robotics and Factories of the Future.; Mandal, D.K., Syan, C.S., Eds.; Springer India: New Delhi, 2016; pp. 207–216.
93. Ahn, D.G. *Directed Energy Deposition (DED) Process: State of the Art*; Korean Society for Precision Engineering, 2021; Vol. 8; ISBN 4068402000.
94. Baxter, I.D. Everse Engineering Is Everse Forward Engineering. **1997**, 104–113.
95. Raja, V. Introduction to Reverse Engineering. *Springer Ser. Adv. Manuf.* **2008**, 1–9, doi:10.1007/978-1-84628-856-2_1.
96. Prof, A. A Review of Reverse Engineering Theories and Tools Ramandeep Singh. **2013**, *2*, 35–38.
97. Villaverde, A.F.; Banga, J.R. Reverse Engineering and Identification in Systems Biology: Strategies, Perspectives and Challenges. *J. R. Soc. Interface* **2014**, *11*, doi:10.1098/rsif.2013.0505.
98. Pham, D.T.; Hieu, L.C. Reverse Engineering–Hardware and Software BT - Reverse Engineering: An Industrial Perspective. In; Raja, V., Fernandes, K.J.,

Eds.; Springer London: London, 2008; pp. 33–70 ISBN 978-1-84628-856-2.

99. Cross, J.H.; Chikofsky, E.J.; May, C.H. Reverse Engineering**Based, in Part, on “Reverse Engineering and Design Recovery: A Taxonomy” by E. J. Chikofsky and J. H. Cross II, Which Appeared in IEEE Software 7(1), 13-17. Copyright IEEE 1990. In; Yovits, M.C.B.T.-A. in C., Ed.; Elsevier, 1992; Vol. 35, pp. 199–254 ISBN 0065-2458.
100. Rekoff, M.G. On Reverse Engineering. *IEEE Trans. Syst. Man Cybern.* **1985**, *SMC-15*, 244–252, doi:10.1109/TSMC.1985.6313354.
101. Chikofsky, E.J.; Cross, J.H. Reverse Engineering and Design Recovery: A Taxonomy. *IEEE Softw.* **1990**, *7*, 13–17, doi:10.1109/52.43044.
102. Otto, K.N.; Wood, K.L. Product Evolution: A Reverse Engineering and Redesign Methodology. *Proc. ASME Des. Eng. Tech. Conf.* **1996**, *4*, 226–243, doi:10.1115/96-DETC/DTM-1523.
103. Ullman, D.G. *The Mechanical Design Process*; Fourth.; McGraw-Hil Companies, Inc.: New York, 2010; ISBN 9780072975741.
104. Anwer, N.; Mathieu, L. From Reverse Engineering to Shape Engineering in Mechanical Design. *CIRP Ann. - Manuf. Technol.* **2016**, *65*, 165–168, doi:10.1016/j.cirp.2016.04.052.
105. Dimas, E.; Briassoulis, D. 3D Geometric Modelling Based on NURBS: A Review. *Adv. Eng. Softw.* **1999**, *30*, 741–751, doi:10.1016/S0965-9978(98)00110-0.
106. Unser, M.; Aldroubi, A.; Eden, M. B-Spline Signal Processing : Part I-Theory. **1993**, *41*.
107. Durupt, A.; Remy, S.; Ducellier, G.; Eynard, B. From a 3D Point Cloud to an Engineering CAD Model: A Knowledge-Product-Based Approach for Reverse Engineering. *Virtual Phys. Prototyp.* **2008**, *3*, 51–59, doi:10.1080/17452750802047917.
108. Ouamer-Ali, M.I.; Laroche, F.; Bernard, A.; Remy, S. Toward a Methodological Knowledge Based Approach for Partial Automation of Reverse Engineering. *Procedia CIRP* **2014**, *21*, 270–275, doi:10.1016/j.procir.2014.03.190.
109. Kumar, A.; Jain, P.K.; Pathak, P.M. Reverse Engineering in Product Manufacturing: An Overview. **2013**, 665–678, doi:10.2507/daaam.scibook.2013.39.
110. Shabani, B.; Pandilov, Z. Analyzing and Application of Reverse Engineering for Design and Developmet Of Mechanical Parts. *Mech. Eng. Sci. J.* **2017**, *35*, 89–96.
111. Chrzan, R.; Urbanik, A.; Karbowski, K.; Moskała, M.; Polak, J.; Pyrich, M. Cranioplasty Prosthesis Manufacturing Based on Reverse Engineering Technology. *Med. Sci. Monit.* **2012**, *18*, 1–6, doi:10.12659/msm.882186.
112. Müller, P.; Gembarski, P.C.; Lachmayer, R. Parametric Topology Synthesis of a Short-Shaft Hip Endoprosthesis Based on Patient-Specific Osteology BT - Towards Sustainable Customization: Bridging Smart Products and Manufacturing Systems.; Andersen, A.-L., Andersen, R., Brunoe, T.D., Larsen, M.S.S., Nielsen, K., Napoleone, A., Kjeldgaard, S., Eds.; Springer International Publishing: Cham, 2022; pp. 669–676.
113. Shih, N.J.; Wang, P.H. Using Point Cloud to Inspect the Construction Quality of Wall Finish. *Proc. Int. Conf. Educ. Res. Comput. Aided Archit. Des. Eur.*

2004, 573–578, doi:10.52842/conf.ecaade.2004.573.

114. Huo, L.; Liu, Y.; Yang, Y.; Zhuang, Z.; Sun, M. Review: Research on Product Surface Quality Inspection Technology Based on 3D Point Cloud. *Adv. Mech. Eng.* **2023**, *15*, 1–17, doi:10.1177/16878132231159523.
115. Yang, Y.; Liu, X.; Kan, C. Point Cloud Based Online Detection of Geometric Defects for the Certification of Additively Manufactured Mechanical Metamaterials. *J. Manuf. Syst.* **2022**, *65*, 591–604, doi:10.1016/j.jmsy.2022.09.011.
116. Guo, J.; Wang, Q.; Park, J.H. Geometric Quality Inspection of Prefabricated MEP Modules with 3D Laser Scanning. *Autom. Constr.* **2020**, *111*, 103053, doi:10.1016/j.autcon.2019.103053.
117. Xu, Z.; Kang, R.; Lu, R. 3D Reconstruction and Measurement of Surface Defects in Prefabricated Elements Using Point Clouds. *J. Comput. Civ. Eng.* **2020**, *34*, 1–17, doi:10.1061/(asce)cp.1943-5487.0000920.
118. Almamou, A.A.; Gebhardt, T.; Bock, S.; Hildebrand, J.; Schwarz, W. Quality Control of Constructed Models Using 3D Point Cloud. **2015**, 20–22.
119. Buswell, R.; Xu, J.; De Becker, D.; Dobrzanski, J.; Provis, J.; Kolawole, J.T.; Kinnell, P. Geometric Quality Assurance for 3D Concrete Printing and Hybrid Construction Manufacturing Using a Standardised Test Part for Benchmarking Capability. *Cem. Concr. Res.* **2022**, *156*, 106773, doi:10.1016/j.cemconres.2022.106773.
120. Puri, N.; Turkan, Y. Dimensional Quality Control of Precast Concrete Slabs Using 3D Laser Scan Point Clouds. *Proc. 16th Int. Conf. Constr. Appl. Virtual Real.* **2016**.
121. Du, L.; Lai, Y.; Luo, C.; Zhang, Y.; Zheng, J.; Ge, X.; Liu, Y. E-Quality Control in Dental Metal Additive Manufacturing Inspection Using 3D Scanning and 3D Measurement. *Front. Bioeng. Biotechnol.* **2020**, *8*, 1–9, doi:10.3389/fbioe.2020.01038.
122. Peuzin-Jubert, M.; Polette, A.; Nozais, D.; Mari, J.L.; Pernot, J.P. Survey on the View Planning Problem for Reverse Engineering and Automated Control Applications. *CAD Comput. Aided Des.* **2021**, *141*, 103094, doi:10.1016/j.cad.2021.103094.
123. Lo Giudice, R.; Galletti, C.; Tribst, J.P.M.; Melenchón, L.P.; Matarese, M.; Miniello, A.; Cucinotta, F.; Salmeri, F. In Vivo Analysis of Intraoral Scanner Precision Using Open-Source 3D Software. *Prosthesis* **2022**, *4*, 554–563, doi:10.3390/prosthesis4040045.
124. Addison, A.C. Virtual Heritage - Technology in the Service of Culture. In Proceedings of the Proceedings of the 2001 conference on Virtual reality, archeology, and cultural heritage (VAST ’01); Association for Computing Machinery: New York, NY, USA, 2001; pp. 343–354.
125. Cignoni, P.; Rocchini, C.; Scopigno, R. Metro: Measuring Error on Simplified Surfaces. *Comput. Graph. Forum* **1998**, *17*, 167–174, doi:10.1111/1467-8659.00236.
126. Shannon, C.E. A Mathematical Theory of Communication. *Bell Syst. Tech. J.* **1948**, *27*, 379–423, doi:10.1002/j.1538-7305.1948.tb01338.x.
127. Blahut, R.E. Information Theory and Coding. In *Principles and Practice of Information Theory*; Middleton, W.M., Van Valkenburg, M.E.B.T.-R.D. for E. (Ninth E., Eds.; Newnes: Woburn, 2002 ISBN 978-0-7506-7291-7.

128. Wilks, S.S. Certain Generalizations in the Analysis of Variance. *Oxford Univ. Press behalf Biometrika Trust* **1932**, *24*, 471–494.
129. Sengupta, A. Generalized Variance. *Encycl. Stat. Sci.* **2004**, 1–11, doi:10.1002/0471667196.ess6053.
130. Droeschel, D.; Stuckler, J.; Behnke, S. Local Multi-Resolution Representation for 6D Motion Estimation and Mapping with a Continuously Rotating 3D Laser Scanner. *Proc. - IEEE Int. Conf. Robot. Autom.* **2014**, 5221–5226, doi:10.1109/ICRA.2014.6907626.
131. Adolfsson, D.; Magnusson, M.; Liao, Q.; Lilienthal, A.J.; Andreasson, H. CorAl – Are the Point Clouds Correctly Aligned? In Proceedings of the 2021 European Conference on Mobile Robots (ECMR); 2021; pp. 1–7.
132. Adolfsson, D.; Castellano-Quero, M.; Magnusson, M.; Lilienthal, A.J.; Andreasson, H. CorAl: Introspection for Robust Radar and Lidar Perception in Diverse Environments Using Differential Entropy. *Rob. Auton. Syst.* **2022**, *155*, doi:10.1016/j.robot.2022.104136.
133. MATLAB, Version: 9.13.0 (R2022b), Natick, Massachusetts: The MathWorks Inc. 2022.
134. Turk, G.; Levoy, M. Zippered Polygon Meshes from Range Images. *Proc. 21st Annu. Conf. Comput. Graph. Interact. Tech. SIGGRAPH 1994* **1994**, 311–318, doi:10.1145/192161.192241.
135. CloudCompare -v2.12 Alpha 2023.
136. Sorokhtin, O.G.; Chilingar, G. V; Sorokhtin, N.O. Structure and Composition of Modern Earth. In *Evolution of Earth and its Climate: Birth, Life and Death of Earth*; Elsevier, 2011; Vol. 10, pp. 13–60 ISBN 1571-9197.

TABLE OF ABBREVIATIONS

Abbreviation	**Definition**
3D	Three-dimensional
AM	Additive Manufacturing
AR	Augmented Reality
AV	Augmented Virtuality
B-Rep	Boundary Representation
CAD	Computer-Aided Design
CAE	Computer-Aided Engineering
CFD	Computational Fluid-Dynamics
CMM	Coordinate Measurement Machines
CNC	Computerized Numerical Control
CT	Computed Tomography
DECI	Differential Entropy-based Compactness Index
DED	Direct Energy Deposition
DICOM	Digital Imaging and Communications in Medicine
DL	Deep Learning
DoF	Degrees of Freedom
EBM	Electronic Beam Melting
EVAR	EndoVAscular Repair
FDM	Fused Deposition Modeling
FEM	Finite Elements Methods
GPS	Global Positioning System
ICP	Iterative Closest Point
IMO	International Maritime Organization
KBRE	Knowledge-Based Reverse Engineering
LiDAR	Light Detection and Ranging
LCI	Low-Coherence Interferometry
LOM	Laminated Object Manufacturing
LS	Laser SIntering
MEX	Material Exstrusion
ML	Machine Learning
MRI	Magnetic Resonance Imaging
NURBS	Non Uniform Rational Basis-Splines
PDF	Probability Density Function
PLA	PolyLactic Acid
RGB	Red-Green-Blue
SLA	Stereolithography
SLAM	Simultaneous Localization and Mapping

STL	Standard Triangulation Language
SVD	Singular Value Decomposition
TOF	Time of Flight
VR	Virtual Reality
WLI	White Light Interferometry